How Anode Porosity affects the performance of a Solid Oxide Fuel Cell

JAKOB BILLEMAR

Department of Applied Physics
CHALMERS UNIVERSITY OF TECHNOLOGY
Göteborg, Sweden 2014

How Anode Porosity affects the performance of a Solid Oxide Fuel Cell
JAKOB BILLEMAR

Department of Applied Physics
Chalmers University of Technology
SE-412 96 Göteborg
Sweden
Telephone + 46 (0)31-772 1000

Chalmers Reproservice
Göteborg, Sweden 2014

How Anode Porosity affects the performance of a Solid Oxide Fuel Cell

JAKOB BILLEMAR
Department of Applied Physics
Chalmers University of Technology

Abstract

The purpose of this project was to investigate how parameters, such as size of zirconia particles and the porosity, impact the performance of the anode of a solid oxide fuel cell. The analysis that has been conducted was focused on investigating SEM-pictures and analysing electrochemical impedance spectroscopy(EIS) measurements on half-cells. The data suggest that an increasing porosity lead to an almost linear increase of TPBs/area in the range of 20-40%. From the results, it was not obvious that the amount of triple phase boundaries(TPBs) was dependent on the size of the zirconia particles in the range between 0.12 and 1μm.

The EIS measurements suggest that the activation energy resulting from the first arc decreased as more measurements were done, at least for the sample named *Red. half-cell*. This effect could be within the margin of errors, and hence just a coincidence. It could also be seen that the sample with the thickest electrolyte gave rise to the highest impedance, but not a much higher activation energy than the other reduced samples. Furthermore there appear to be a difference in shape between reduced and not reduced samples, and a substantial differences regarding activation energy and conductivity could also be seen.

Keywords: SOFC, TPB, EIS-measurements, YSZ, Ni, NiO, SEM-picture, porosity, particle size, anode, half-cell

Acknowledgements

This is a master's thesis work of 30 credits in applied physics from Chalmers University of Technology. I am very thankful for the support from my supervisors Johanna Stiernstedt and Bengt-Erik Mellander, who have helped me throughout the project with everything from discussion of results to production of samples and other measurement data.

Jakob Billemar, Göteborg 2014-06-09

Contents

List of abbreviations

SOFC	Solid Oxide Fuel Cell
TPB	Triple-phase-boundary
V	Voltage
AC	Alternating Current
DC	Direct Current
I	Current
R	Resistance
Z	Impedance
EIS	Electrochemical Impedance Spectroscopy
A	Area
kW	kilowatt
MW	Megawatt
C	Capacitance
i	Current density
Ni	Nickel
YSZ	Yttria-Stabilised Zirconia
SEM	Scanning Electron Microscope
H_2	Hydrogen
CO_2	Carbon dioxide
CO	Carbon monoxide

1 Introduction

In this section a short introduction to this work is given. The section is divided in three subsections, namely background, purpose and scope. These three subsections will present why this is interesting and what the purpose of this project is.

1.1 Backround

One of the hottest topics the last years has been the changing environment, and especially the increased green house effect through an increased net emission of green house gases, like carbon dioxide, CO_2 [1]. Maintaining this behaviour is not sustainable and will not work in the long run. Measurements suggest that the temperature is increasing, and at an increasing rate [1]. To transit into a more healthy future several changes need to be taken.

A good alternative that potentially could replace todays petrol and diesel engines are different types of fuel cells; fuel cell is a device that is able to convert chemical energy to heat and electrical energy, with very high efficiency [1,2]. This alternative would also lower the exhaust of nitrogen oxides and sulphur oxides [3]. Fuel cells are rather flexible energy converters and can be used in various different applications, and at the same time combined with renewable energy sources [4]. One of the most interesting applications is the so called regenerative fuel cell, which is basically a fuel cell that can run the backward reaction [5]. Possible applications range from small residential applications with a power of 1-5 kW, up to power plants with aim to deliver enough energy for a whole region, these applications need 100-300 MW [4].

The first fuel cell was invented in 1839 by Sir William Grove [6], so it is not a very new innovation. The early development of fuel cells was quite slow [7]. For many years the evolvement of fuel cells was almost zero, due to high cost, but the development started again with the oil crisis [7].

One of the most promising types of fuel cells is the Solid Oxide Fuel Cells (SOFC) [1]. This is because SOFCs are not as damaging to the environment as other energy converters, or at least it can be if the fuel is produced in an environmentally way [4], while also being characterised by a very high efficiency [8], of as high as 70%(or even 90% if the heat is used) [1]. There are already SOFCs on the market, directed for local and emergency application [9].

1.2 Purpose

The purpose of this work is to investigate the effect of mainly porosity, but also other parameters like size of zirconia particles, on performance of the anode in an SOFC. In order to achieve this a literature study was conducted before analysis of real samples, delivered by Swerea, were performed. SEM-pictures of the samples were investigated with respect to porosity and number of Triple-phase-boundary(TPB)-points. After

the analysis of the SEM-images, some half-cells were further analysed by Electrochemical Impedance Spectroscopy(EIS). The experimental work had been done by the supervisor Johanna Stiernstedt, and most of it before this project started.

1.3 Scope

In the project, only the properties of the anode have been investigated. Furthermore, only the number of triple-phase-boundaries has been investigated as a measure of the performance of the fuel cell. In the section concerning electrochemical impedance spectroscopy, the activation energy has mainly been investigated.

2 Theory

In this part the most important theory related to the work is presented. The theory section has two main parts. The first deals with the theory that concerns solid oxide fuel cells and the second part deals with theory regarding electrochemical impedance spectroscopy.

2.1 Solid Oxide Fuel Cells

2.1.1 Parts of the cell

A solid oxide fuel cell(SOFC) is built by the following important active parts: cathode, anode and solid electrolyte [8], where the electrolyte is separating the anode from the cathode [2]. A schematic picture of a fuel cell can be seen in figure 1. In this figure, H_2 is used as fuel, O_2 as oxidant and H_2O is the product. There are different types of SOFCs, called sealless tubular design, segmented-cell-in-series design, monolithic design and flat-plate design [2]. The fuel cell uses the energy from a chemical reaction between a fuel and an oxidant and converts that energy into heat and electricity [2].

Ni/YSZ, where YSZ stands for yttria-stabilised zirconia and Ni stands for nickel, is a common anode material in SOFCs [2]. Ni is used since it is durable at the required high operating temperature and cheap as well, while YSZ is used due to its stability and oxygen-ion conductivity [2]. YSZ is a common material used as electrolyte [2], this material is an oxygen-ion conductor [8]. The cathode material can only be made of very specific material, due to the very high temperature, for example noble metals and electronic conducting oxides such as platinum [10] and doped lanthanum manganite [2]. Another example of material used for anode, electrolyte and cathode, that potentially could be used for future applications are anodes based on $LaCrO_3$, electrolyte based on ceria and Ba-based perovskite-type oxide as cathode [9].

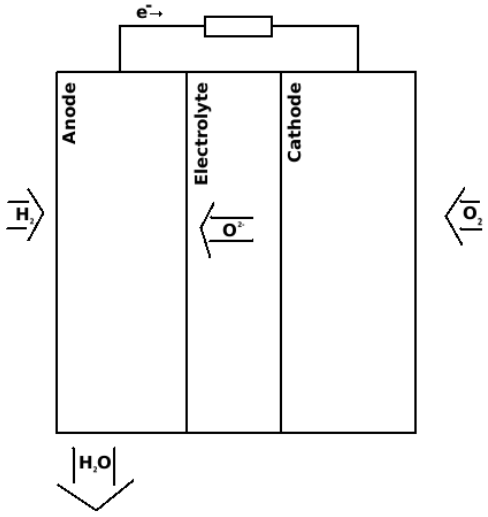

Figure 1: Schematic picture of a fuel cell. The hydrogen is fed from the left into the anode, the oxygen is fed from the right into the cathode. The product is water in this case. This picture is valid for an oxygen-ion conducting electrolyte, like YSZ.

2.1.2 Fuels

The most common fuel for the SOFC is hydrogen(H_2), but also carbon monoxide(CO) can be used as fuel [11], together with almost any combustible fuel [3]. SOFCs are very flexible when it comes to fuel, the major reason for this is that oxygen ions are transported in the electrolyte [3]. CO can actually be used both directly or be reformed to hydrogen and carbon dioxide [12]. Hydrogen is good to use as fuel due to its high electrochemical reactivity [13].

The high operating temperature in SOFCs can be used to reform hydrocarbons, this implies that the fuel cell can be fed with hydrocarbons(good since handling of hydrogen is complex and not cheap to extract [1]), which can be reformed to hydrogen, carbon dioxide and carbon monoxide, through the following chemical reactions [13]:

$$CH_4 + H_2O \rightarrow CO{+}3H_2 \tag{1}$$

$$CO{+}H_2O \rightarrow CO_2 + H_2 \tag{2}$$

Both these chemical reactions are endothermic and can be catalysed by nickel [13]. Hydrogen and carbon monoxide react with oxygen exothermically according to the following two chemical reactions(for anode, cathode and total respectively) [11]:

$$\begin{aligned} &\text{Anode: } 2H_2 + 2O^{2-} \rightarrow 2H_2O + 4e^- \\ &\text{Cathode: } O_2 + 4e^- \rightarrow 2O^{2-} \\ &\text{Total: } 2H_2 + O_2 \rightarrow 2H_2O \end{aligned} \tag{3}$$

$$\begin{aligned} &\text{Anode: } 2CO{+}2O^{2-} \rightarrow 2CO_2 + 4e^- \\ &\text{Cathode: } O_2 + 4e^- \rightarrow 2O^{2-} \\ &\text{Total: } 2CO{+}O_2 \rightarrow 2CO_2 \end{aligned} \tag{4}$$

CO can, as can be seen in the chemical reactions (4) and (2), either be used directly or reformed into hydrogen and carbon dioxide [12]. The chemical reaction in (2) is called the water-gas shift reaction [13].

2.1.3 Stack designs

There are several techniques that can be used to fabricate the different parts of the SOFC. There are four different designs, namely sealless tubular design, flat-plate design, monolithic design and segmented-cell-in-series [2]. These designs have different advantages and disadvantages. For example, planar fuel cells have a higher theoretical performance than tubular [14] and segmented-cell-in-series designs [2]. The highest power densety has the monolithic design, since it has a low resistance [2]. The sealless design is advantageous in the matter that it is not as sensitive to thermal shocks as the other designs, due to the geometry of the design [14].

2.1.4 Fuel Cell system

In a fuel cell system, there is much more than just the fuel cell [4]. The following parts are quite common in a fuel cell system [4]:

- Fuel and oxidant provider (and sometimes fuel processing system)
- DC-to-AC-converter
- System to remove impurities
- System that control the temperature of the cell
- System that removes the reaction product

The cell in the system usually does not take more space than approximately 1/3 of the total volume, the rest of the space is taken up by the different subsystems mentioned above in the list [4].

2.1.5 Tape casting

Tape casting is one of the techniques that can be used in the fabrication of fuel cells [15]. This method has been used in the production of the samples in this work. Tape casting can be used to produce thin samples of ceramic materials [16]. One of the positive things with tape casting is that it can be used in the industry, which is done for example at Topsoe Fuel cell [15], due to the possibility of mass production [17], and that it is not too expensive [16]. The tape casting process begins with the mix of a slurry of ceramic powder mixed with binder, solvent, dispersing agent and plasticiser, which is then put in a machine [16]. In the machine the slurry is evenly spread out as a thin layer(tape) on a carrier film [16]. When this tape is dry it can be formed into the desired shape, after this step the binder needs to be burnt out before finally being sintered at a high temperature [16]. Examples of other techniques that can be used are tape calendaring, sputtering, spin coating and plasma spraying [17].

2.1.6 Performance

The main idea with fuel cells are that they are using a chemical reaction and transforms this reaction's Gibbs free enthalpy into electricity [18]. The maximum theoretical voltage, E, that can be created for a certain pressure at the cathode and the anode of the cell comes from the relationship called Nernst equation:

$$E = (RT/2F) \log \frac{P(O_{2,cathode})^{1/2}}{P(O_{2,anode})^{1/2}} \tag{5}$$

where F is Faraday's constant, R is the gas constant, T is the temperature in kelvin and P denotes the pressure [3]. It should be noted that since oxygen is not fed to the anode, $P(O_{2,anode})$ is determined by an equilibrium relationship which depends on the fuel used [3].

Measuring the performance of a fuel cell, one can draw conclusions where some of the losses origin from, this can be done by measuring the voltage and current relationship, these measurements usually give data like that in figure 2 [19].The figure shows data measured for three different PEM-cells during a laboration in a fuel cell course. From this graph four different regions are usually discussed, namely activation losses, fuel crossover and internal currents, ohmic losses and concentration losses, these losses stem from different phenomena in the cell [20]. Ohmic losses come from all the resistances that exist in the cell, both ionic- and electronic-resistance [20]. When the cell is operated at high current the concentration losses are apparent, this loss comes from the fact that the supply of fuel and oxidant is limited in the porous anode [19, 20]. Fuel crossover and internal currents come from the fact that the fuel may pass through the electrolyte and react with oxygen at the cathode instead, or that the electrolyte may have some electronic conduction, both these processes leads to losses in performance [20]. The activation losses come from the fact that some energy is needed to activate the cell [20]. These losses are

less apparent when the cell is operated at a higher temperature [20]. The temperature in SOFCs are usually very high, and consequently they have no big losses in this activation region, but when the temperature increases, the theoretical efficiency maximum is lowered [20].

The following equation describes approximately how the previously mentioned losses are affecting the voltage for different currents [20]:

$$\begin{aligned} V =& E - \Delta V_{\text{resistance}} - \Delta V_{\text{activation}} - \Delta V_{\text{concentration}} \\ =& E - ir - A \log \frac{i + i_n}{i_0} + me^{ni} \end{aligned} \tag{6}$$

where V is measured voltage, E is the maximum voltage, i; current density, i_n; the current density that matches the losses from internal and fuel crossover, A; Tafel slope and i_0; exchange current density. Further, m and n are constants that are fitted to data in order to model the concentration losses and r is the area-specific resistance [20]. E in equation (6) can be calculated by using the equation (5).

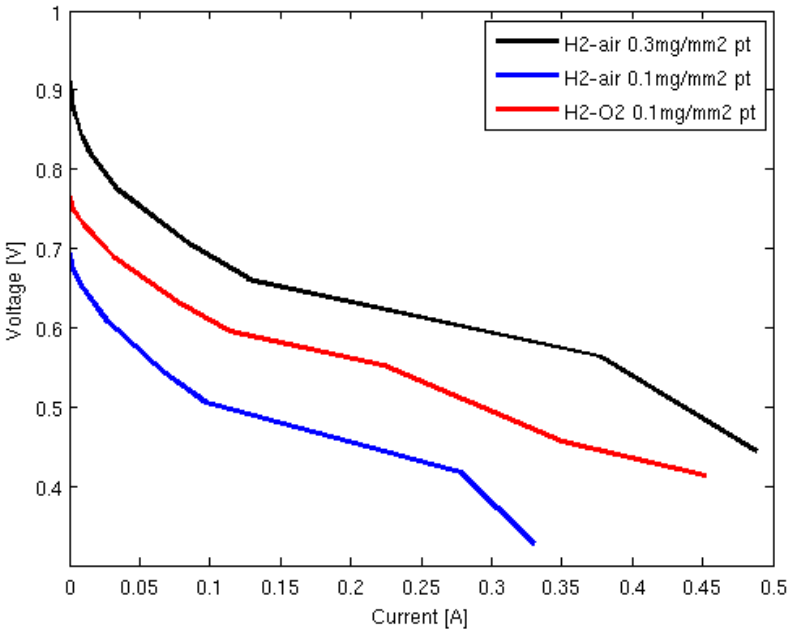

Figure 2: I-V-relationship for three different PEM-cells.

The power of a cell is also usually plotted together with the I-V-plot, as has been done by for example Suzuki *et al.* and Lee *et al.* in the following articles [9] and [21], respectively. An example of such a plot can be seen in figure 3. This figure is for the same PEM-setups as in figure 2, and the data were collected during the same laboration. Depending on how large the different losses are, the relationship between power and current will be different which can be realised by studying equation (6). From the I-V-relation, the power graph can be calculated by plotting the

voltage multiplied with the current [22], and then plot the current against the power.

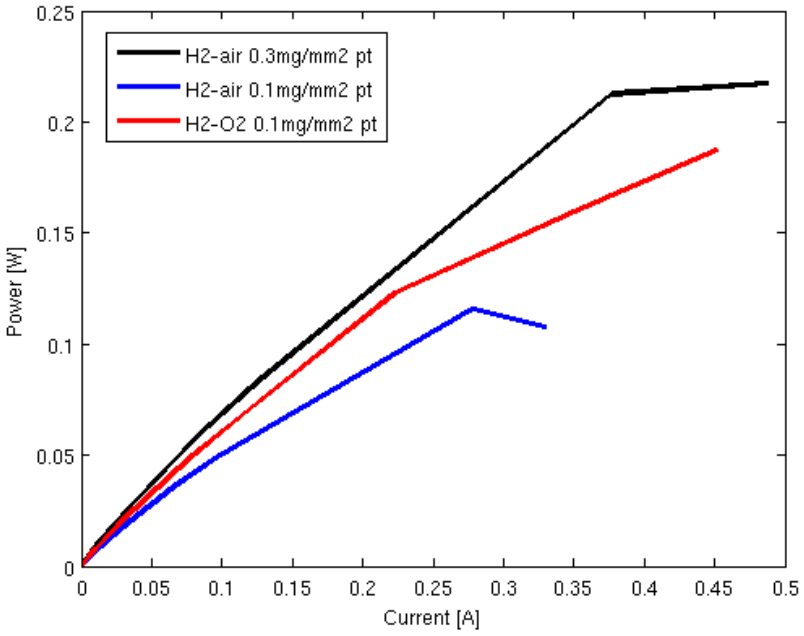

Figure 3: Measured relationship between current and power for the same three PEM-cells as in figure 2.

2.1.7 Charge double layer

Another important factor that needs to be explained in order to get a better picture of the fuel cell's dynamic electrical behaviour, is the charge double layer. A charge double layer is always created at the interface between two different materials, and created through several effects, like diffusion, applied voltages and electronic and ionic reactions [20]. A schematic picture of a charge double layer can be seen in figure 4.

As all separation of charge, the charge double layer will create a voltage difference [23], and a potential difference that can be interpreted as the activation loss [20], mentioned earlier in the text. When charges are separated in this manner, the setup will form a type of capacitor, where the capacitance, C, is the ratio between charge, Q, and potential difference, V. [23].

$$C = \frac{Q}{V} \tag{7}$$

By estimating the capacitance as that of a parallel plate capacitor, the formula below can be used to calculate the capacitance, which then can be used in an equivalent circuit to model the behaviour of the cell [20].

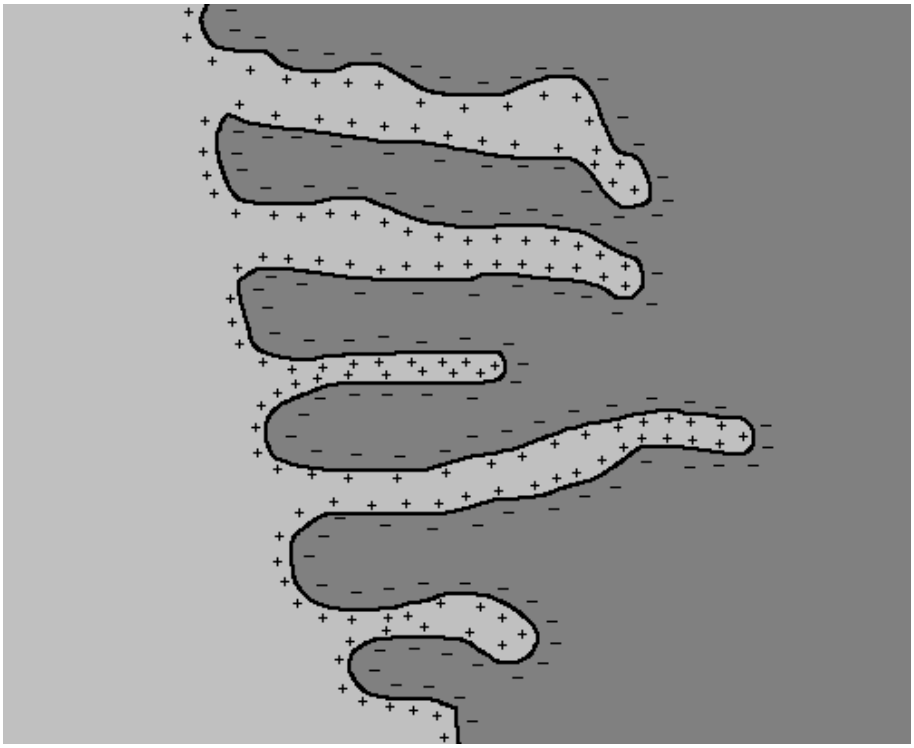

Figure 4: Schematic figure of a double layer.

$$C = \epsilon \frac{A}{d} \tag{8}$$

In the formula above, A is the area, d is the distance between the two imagined plates and ϵ is permittivity of the medium separating the two plates [20, 23]. In the case of fuel cells the capacitance may be quite large, this since the area is the total surface area of the interface between electrode and electrolyte and the distance between them is really small [20]. The dynamic behaviour of the fuel cells is thus smooth when the voltage is changed for the fuel cell, since a capacitor has this behaviour [20].

2.1.8 Characterising properties

One characteristic property of SOFCs is the very high operating temperature, often around 700 ^{o}C or above [9, 11]. Because of the high operating temperature, non-precious metals can be used as catalyst, like nickel(Ni), which is both stable and has high electronic conductivity [2, 11]. Another positive effect that stems from the high temperature and the use of Ni is that it is feasible to internally reform hydrocarbons, like natural gas [11, 13], or used in a steam turbine to further enhance the efficiency [3].

The high temperature also lead to some disadvantages. One of these disadvantages is that SOFCs demand quite special properties of the materials [9] to sustain

its function for a reasonably long time [11], for example almost all materials oxidise quite easily at this high temperature [24]. One example of the problem with the high temperature is that there can be diffusion of the transition metals used in the electrodes into the electrolyte [9]. The very high temperature also leads to high stresses if there exists a mismatch in thermal expansion [12]. Another disadvantage is that a higher operating temperature means a longer start-up time [9].

There are several properties characterising an SOFC that have an impact on the performance. One of the more important properties is the porosity, which affects several other properties of the ceramic anode material, for example mechanical strength and ionic- and electronic-conductivity [25]. The level of porosity affects the performance, and the optimal porosity is around 40% [8]. Ni-YSZ does not normally has this porosity, some sort of poreformer needs to be added [21]. Examples of these poreformers are graphite [21], cornstarch [26] and potato starch [27]. It has been seen by for example J.-H. Lee *et al.* [21] that it is not always just the porosity that matter when it comes to gas permeation, but rather the effective porosity. The effective porosity is defined as all the porosity except "dead ends" and "ink bottles" [21].

Another important property of the anode that affects the performance of the SOFC is the so called triple-phase-boundaries(TPB), which are points(in 2D) or lines(in 3D) where electrolyte, pore and catalyst meet [28]. These areas are important since it is at these points the reactions take place [19]. J. Divisek *et al.* found a direct correlation between the amount of TPBs and the electrochemical exchange current density in their article "Structure investigations of SOFC anode cermets Part I: Porosity investigations" [28]. One method to determine the number of TPB in an anode is to count them by hand or with the help of a software after a proper image has been taken, this has been done by, for example, Divisek and Wilkenhöner [28] and by Lee *et al* [8]. It has been seen that the TPB that is closest to the electrolyte is where most of the reactions happen, this area is sometimes called the reactive zone [19] and different depths of this regions has been reported, for example 40-50μm [10] and approximately 10μm [19] from the electrolyte surface. The depth of the reactive zone is dependent on the ionic conduction of the cermet, this because it is energetically favourable for the oxygen ions to react chemically at the surface, and thus be depleted [19]. This means that the better the ionic conduction is, the further the oxygen ions can be transported into the anode before reacting. All TPBs are not necessarily active even if they are located in the reactive zone, the reason for this is that the different phases need to be connected all the way to the reactive sites [3].

When hydrogen is oxidised, water vapour is created. This water vapour leaves the surface near the place where it has been created, thus the active TPBs [19]. Before it desorbs from the TPBs it is preventing H_2 from adsorbing on the active part, this problem is more apparent at higher currents than at lower [19]. The hydrogen may be adsorbed at sites some distance from a TPB, but it is not possible for it to react with oxygen-ions, since to be able to react with these ions, the adsorbed hydrogen needs to surface-diffuse to the TPB [19].

In the article "Impact of Anode Microstructure on Solid Oxide Fuel Cells" by Toshio Suzuki *et al.*, they report that their data suggest that the size of Ni particles are affecting the performance of the SOFC, by improving the microstructure of the anode [9]. They also think that the size of the Ni particles is an extra important factor for lower operating temperatures [9].

2.2 Electrochemical Impedance Spectroscopy

One of the methods that are used to study fuel cell materials is the electrochemical impedance spectroscopy(EIS) [20]. To get a better understanding of the basic idea, a short review of the most important parts of the theory is presented. The simplest case of impedance is that of an ideal resistor in a circuit with direct current, in this case the resistance R, can be written as follows(where V is voltage and I is the current.): [7].

$$R = \frac{V}{I} \tag{9}$$

In real systems the impedance depend on several different processes, like the electrochemical double layer, diffusion and so on [7]. In these more complicated system, like fuel cells, one can use the following equation to find how the impedance is dependent on frequency:

$$Z(\omega) = \frac{V(t)}{I(t)} \tag{10}$$

In the equation above, $Z(\omega)$ is the impedance at a certain frequency, and $V(t)$ and $I(t)$ is the voltage and current, respectively, measured by an alternating current [7]. The resulting impedance, $Z(\omega)$ can be represented by a complex number, with real part and imaginary part, or as a vector in the complex plane [29].

The resulting spectrum from the measurements is usually plotted as functions of frequency in Nyquist and Bode diagrams, where a Nyquist plot shows how the imaginary part vary with the real part for different frequencies, and a Bode plot show either (the logarithm of) the absolute value of the impedance against the logarithm of frequency or the phase angle against logarithm of the frequency [30]. Examples of how these two plots can look like are shown in figure 5. Of these two different plots, the Nyquist plot is the most common to use when analysing a sample [30], example of publications where the authors have used Nyquist plots to visualise their results are the following articles by Kong *et al.* [10] and Suzuki *et al.* [9].

In a Nyquist plot, an ideal resistor will look like a single dot on the real-axis, the x-value will be the resistance, an ideal capacitor will have different points along the y-axis, depending on the frequency, the y-value will change according to $\frac{1}{\omega C}$, this line is translated in the positive x-direction if an ideal resistor is connected in series with this capacitor [29]. If the resistor is connected in parallel instead, the points will be

distributed on a half circle, with end-points at the origin and at the x-axis with the same value as the resistance [29]. These three examples can be seen in the figure 5, with its corresponding Bode-plot. In the figure, the plots to the left are Bode-plots and the plots to the right are the corresponding Nyquist-plot, the plot in the top shows the result from an ideal resistor, the plots in the middle represents the result from an ideal capacitor, and finally the plots in the bottom displays the result from a circuit with an ideal resistor and an ideal capacitor in parallel. Often when an EIS analysis has been conducted an equivalent circuit for the data is sought [29, 30].

EIS is a technique that does not require that the sample is destroyed in any way, which make it suitable to investigate time dependent properties and evolution of the system [31]. The technique is expensive, and this is one of the major disadvantages [31]. When the capacitance and resistance have been extracted from the EIS-data, the resistance is modelling the processes related to charge transfer and the value of the capacitance comes from charge separations, like double layers [32]. One phenomena that can be seen in the EIS-spectrum is the Warburg impedance. Warburg impedance give rise to linear increase of the impedance in a Nyquist plot, the linear increase is equal to y=x [32]. Physically Warburg impedance comes from mass transport diffusion phenomena in the sample [32].

From EIS-measurements, the resistance that controls the ohmic losses in the polarization curve can be extracted [33]. The value that should be taken is the real value when the frequency goes to zero [33].

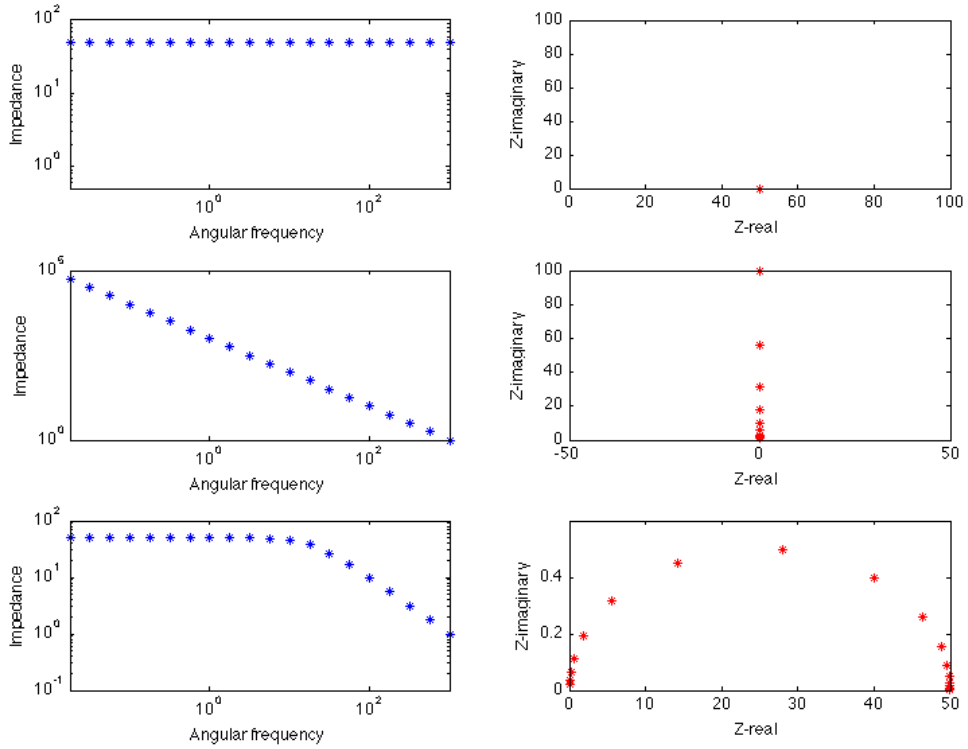

Figure 5: On the left hand side the Bode-plot for three different electrical circuits are showed. On the right hand side the respective Nyquist-plot is shown for comparance. The different circuits are, from top and down: an ideal resistance, an ideal capacitor and an ideal capacitor in parallel with an ideal resistor.

3 Method

In this section a brief presentation of the different methods used will be explained. The order that the different methods are presented in shows how central they are in the project. The main focus of this section is in presenting the practical work and the analysis that have been conducted.

3.1 Literature study

In order to achieve the right theoretical knowledge about SOFCs in general and the anode of the SOFCs in particular a literature search was conducted in the beginning of this project. The main part of the literature search has been conducted in the library and on the home page of the library. Some articles and other references has been investigated also during later parts of the project.

3.2 Naming the samples

In this report quite a few samples have been analysed. For the convenience of the reader, a short section about how they are named is presented here.

3.2.1 Anode samples

All the different anode samples in this project have been named in the following way: The first part of the name says what elements are included in the anode, in this report all the anode samples are made of nickel(Ni) and zirconia(ZrO_2). The next part of the name indicates the ratio they are mixed in, for example (50/50) mean the same amount of each by volume. The last part of the name says when they were done (if they are done the same day they are separated with a letter). The different anode samples that have been analysed can be seen in table 1, together with some properties of the samples.

Table 1: Names and some properties of the anode-samples that were investigated.

Name	**Binder** [%]	**Starch** [*type* & %]	**Zr size** [μm]
Ni/ZrO_2(50/50) 050613	25	corn 35	0.68*
Ni/ZrO_2(50/50) 230513	25	corn 40	1.0
Ni/ZrO_2(50/50) 220911	25	potato 35	0.12
Ni/ZrO_2(30/70) 120913	25	corn 30	0.12
Ni/ZrO_2(50/50) 180613	25	corn 35	0.57*
Ni/ZrO_2(35/65) 230413	25	corn 35	1.0
Ni/ZrO_2(50/50) 010414A	25	corn 22	0.36
Ni/ZrO_2(50/50) 010414B	25	corn 40	0.36

*bimodal Zr-particle size distribution (mixture of 0.12 and 1 μm.)

3.2.2 Half-cell samples

Later in the report when EIS-measurements are analysed, a new set of samples are studied. These samples are all half-cells, meaning that they consist of both an anode and an electrolyte. In this report three different reduced half-cell samples are analysed, they are named *Red. Half-cell*, *Thin electrolyte* and *Thick electrolyte*. Several different EIS-measurements have been conducted on these samples and to separate them, they are named after the date the experiments were conducted. For example 060911, 063011 are experiment that were done on the cell *Red. half-cell*. Which measurement that belong to which sample can be seen later. One half cell that was not reduced was also analysed and it is called *Not reduced*.

3.3 Finding porosity

The open porosity of the anode samples were found using three measurements. The first measurement was weighing the sample when it was dry, next the sample was weighed under water and finally the sample was weighed when wet. By the use of Archimedes' principle the open porosity can, for example, be found from these measurements.

3.4 Analysis of the SEM-pictures of the anode

During this work an analysis of eight anode samples has been conducted in two rounds. In the first round six samples were analysed and then after this analysis two more samples were prepared at Swerea and analysed at Chalmers. This second round of samples were produced and analysed to verify some interesting correlations, more about this in the results. The SEM-pictures of the samples can all be seen in figure 6.

Three different half-cells were also investigated with respect to the same parameters as for the anode samples. SEM-pictures of the three samples that were investigated can be seen in figure 7. The thinner region at the top of each of these samples is the electrolyte, and the thicker part is the anode.

The analysis has been done with respect to the following properties, amount of TPBs, length of the path where TPBs are possible, the area of pores and the area of the analysed region. An example of one of the SEM-pictures that was analysed can be seen in figure 8. In the figure the black parts are pores, the lighter grey parts are zirconia, ZrO_2 and the darker grey parts are nickel, Ni.

If we magnify this picture around the specified area in the red rectangle, the image in figure 9 can be seen. In this figure the three different regions can be seen more clearly. The amount of TPBs is equal to the number of regions where all these three phases meet, and all these appear along the boundary of the pores. In the figure, two TPBs have been marked by red circles.

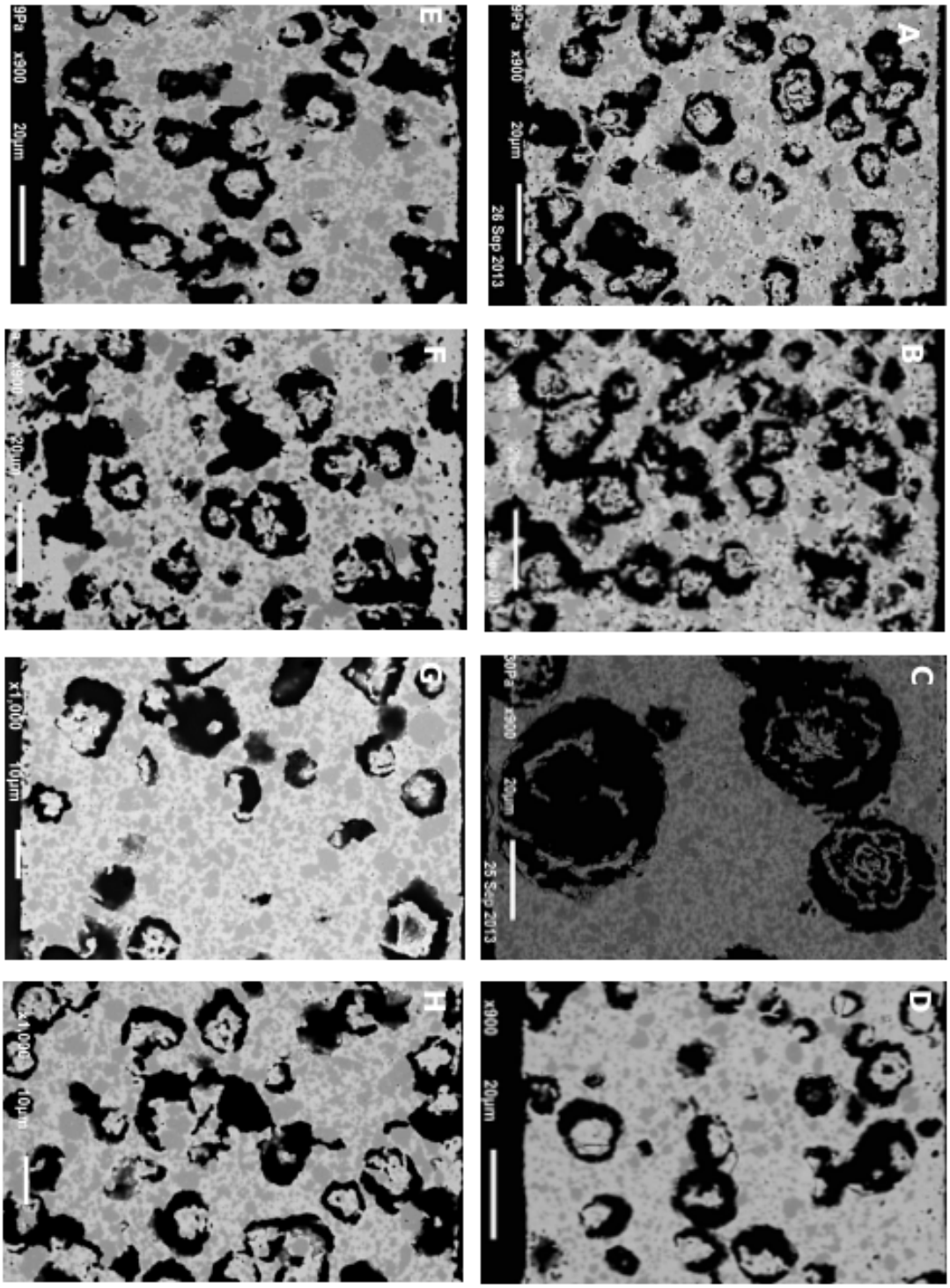

Figure 6: SEM-pictures of all eight anode samples. The SEM-pictures are ordered in the following way(first part of the names has been omitted): A) 050613, B) 230513 C) 220911 D) 120913 E) 180613 F) 230413 G) 010414A H) 010414B

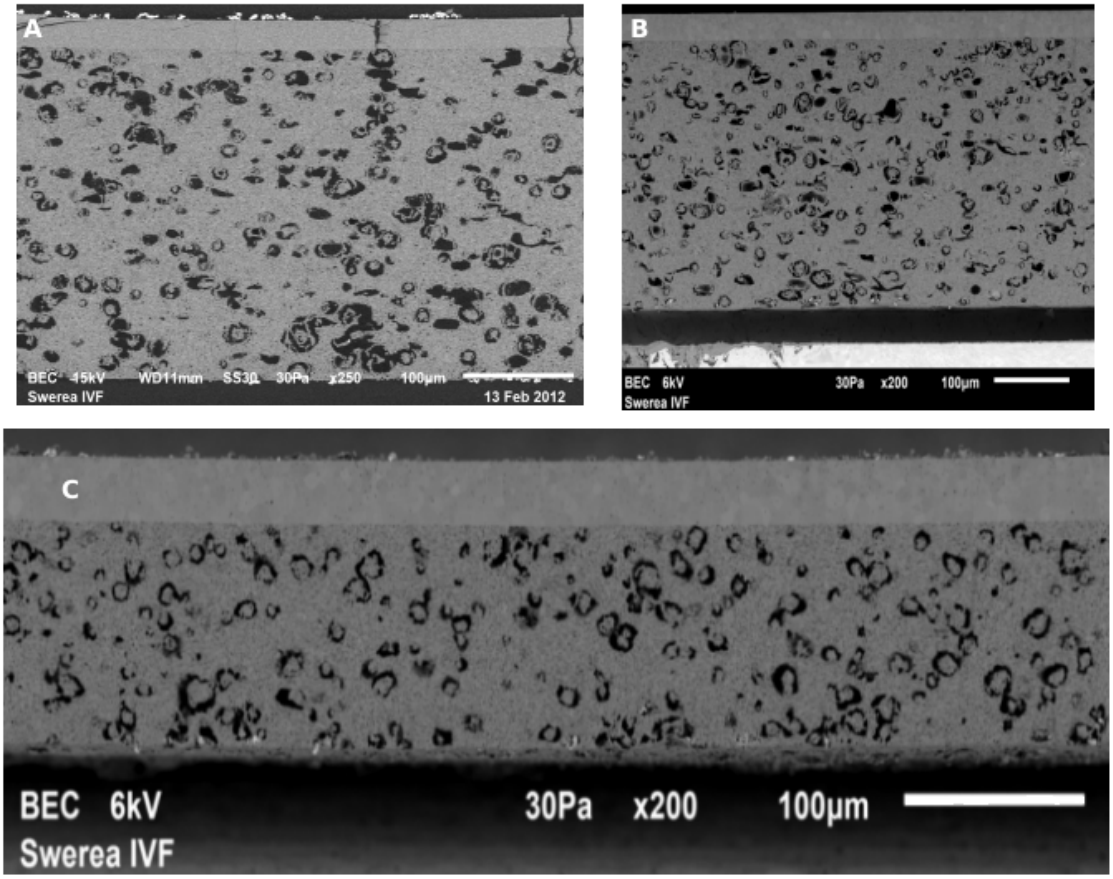

Figure 7: SEM-pictures of all three half-cell samples. SEM-pictures are ordered in the following way: A) Red. halfcell , B) Not reduced and C) Thin electrolyte

For the first set of six samples the area of the pores, as well as the circumference of them were first measured and calculated without help from any software, and later verified with the software FIJI. Before calculations were done, a region that could be considered to represent the whole sample were chosen. How many TPBs for each pore, what circumference and area of each pore were noted.

For the second set of samples the same measurements were done. The area and circumference were measured with the aid of the software FIJI. In FIJI a certain value of the grey-scale need to be chosen to calculate the porosity. It was hard to know exactly what value should be used. The brightness of the samples varied quite much so the same value could not be used for all the different samples. A slight change in this value could give a few percent change of the porosity. The method that was used to determine the value was to take an as high value as possible without the software counting regions that clearly was not pore. Examples of different values of greyscale can be seen in figure 10 for sample 220911, the red area in the figure is the part that the software is counting as pore. In the figure to the right it

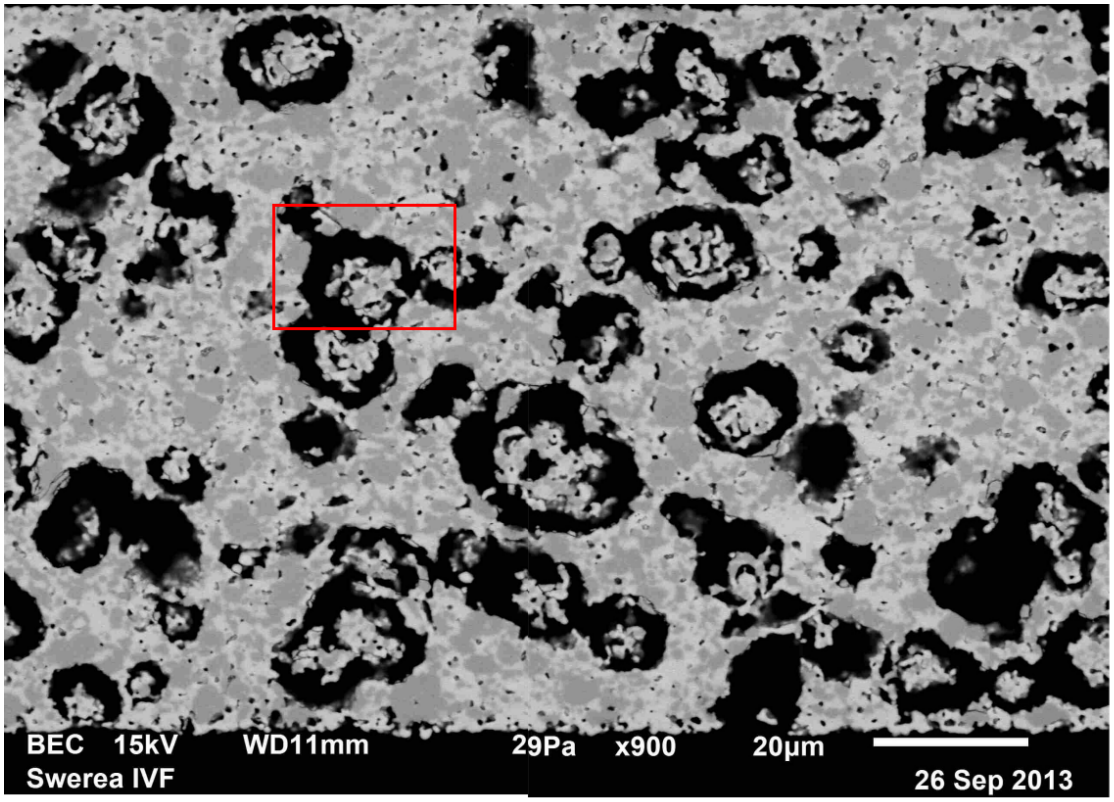

Figure 8: SEM-picture of the anode sample named Ni/ZrO_2(50/50) 050613.

can clearly be seen that the software is counting areas that should not be counted as pore, while the figure to the left has a good value. Since this method has been used, the value of the area-porosity is probably a bit higher than what it really should be. If the pores are well distributed in the sample and a big enough part of the sample is analysed, the area porosity should be quite close to the real porosity. To use this method with greater precision, several cross sections of the same sample should be analysed.

For all of the first six samples, except sample NiZrO_2(30/70) 120913, the open porosity was measured. This was not done for the last two samples. Instead, the porosity was approximated by the use of FIJI for a big piece of the sample.

3.5 Design of new samples

After the measurements and analysis of the first six samples had been done, two more samples were made based on observations of the first six. There seemed to be a quite linear relationship between the size of the zirconia particles and the amount of TPBs per μm of the pore boundary. These results will be presented in more detail in next section, but mentioned here as an argument for the desired properties of the new samples. This could also be motivated from the results of Suzuki

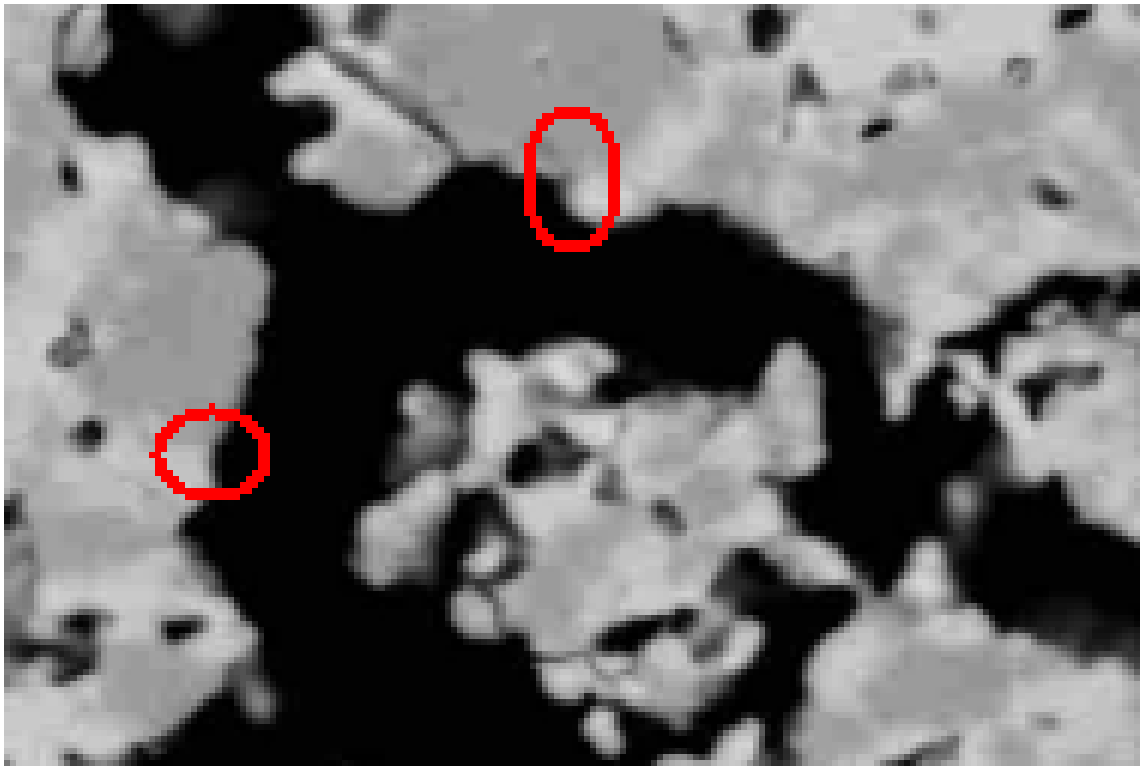

Figure 9: A magnified region of the anode sample Ni/ZrO_2(50/50) 050613.

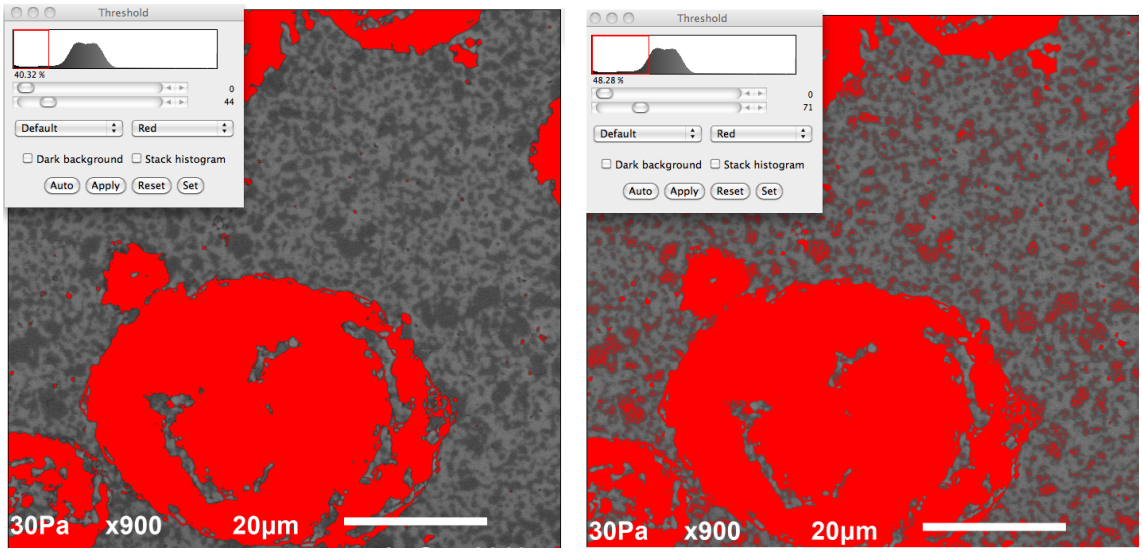

Figure 10: In the figure to the left a high, but good value has been chosen. In the figure to the right a too high value has been chosen. In both figures, the sample Ni/ZrO_2(50/50) 220911 is displayed.

et al. [9] where they noticed that the Ni particle size influenced the performance. Another interesting trend that was seen in the first six samples and further investi-

gated with the last two samples, was that the TPB per area vs open-porosity looked linear. This was the motive to make the last two samples in the way they were done.

3.6 Electrochemical Impedance spectroscopy

Electrochemical Impedance Spectroscopy(EIS) was used to analyse the samples, over a range of temperatures. At each temperature the impedance was measured at several different frequencies.

3.6.1 Measurement

The experimental data were gathered by the use of a special experimental setup. A schematic picture of the experimental setup used for the measurements can be seen in figure 11. In this figure the two different thermocouple are used to monitor the temperature in the oven and of the sample, the platinum paint on the samples are there to ensure a better contact between sample and platinum electrodes. When the samples has been put in place and the proper settings been decided with respect to temperature and frequencies, the measurements begin. To get the desired temperature, the experimental setup is put in an oven. The samples are connected to the setup by platinum contacts. For the samples analysed in this report the setups were chosen as stated in table 2. During the measurement, the oven heats the sample to a certain temperature, and when this temperature has been reached, the impedance is measured at discrete frequency points. This step is repeated for the temperatures of interest.

Table 2: Setups for different EIS measurements

Name	**T interval** $[^oC]$	**Frequencies per decade**	**F interval** $[Hz]$
052011	281.1-622.2	10	$5 - 13 \cdot 10^6$
060911	481.3-646.5	10	$5 - 13 \cdot 10^6$
063011	277.9-602.4	10	$5 - 13 \cdot 10^6$
070111	373.9-605.7	10	$5 - 13 \cdot 10^6$
081811	29.4-774.0	10	$5 - 13 \cdot 10^6$
120811	349.2	10	$5 - 13 \cdot 10^6$
121611	378.1-709.3	10	$5 - 13 \cdot 10^6$
012012	275.3-691.9	10	$5 - 13 \cdot 10^6$

3.6.2 Analysis of the EIS data

The results from EIS measurements are, in this report, shown as Nyquist plots of the impedance for each temperature. From all these plots one can extract data to get the conductivity and the activation energy. The activation energy can be found by plotting the logarithm of the conductivity against one over the temperature, where the slope is equal to $-E_a/R$, where R is the gas constant and E_a is the activation

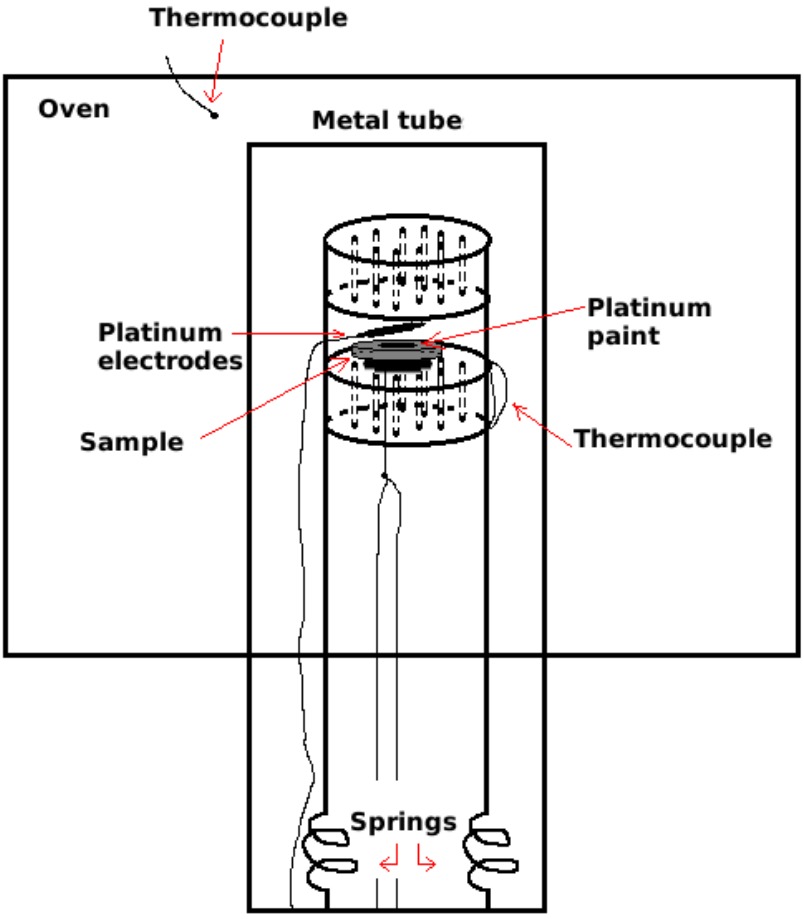

Figure 11: Schematic picture of the EIS-experimental setup, drawn from a sketch made by the supervisor Johanna Stiernstedt.

energy per mole in joule.

The conductivity is given by

$$\sigma = \frac{l}{AR} \tag{11}$$

where A is the cross-section area, l is the thickness and R is the resistance of the sample [22]. The only quantity that can vary with the temperature is the resistance. The resistance can be found from the plots that show the relation between the real and imaginary part of the impedance (Nyquist plot). At most one value of the resistance should be picked from each of the arcs in those plots, and the value that should be picked is the real value of the local minimum, shown in figure 12, thus 6123 Ω in this case. The marked dot in this figure is the one that should be used as resistance for this temperature and arc. This minimum is not always easy to find. Sometimes an equivalent electric circuit need to be used that gives approximately the same behaviour as the measured one. One example of a circuit that quite often is used is a more or less complicated system of a resistor in parallel with a capacitor,

where the impedance looks like the bottom plot in figure 5, and then use the resistor value as the resistance.

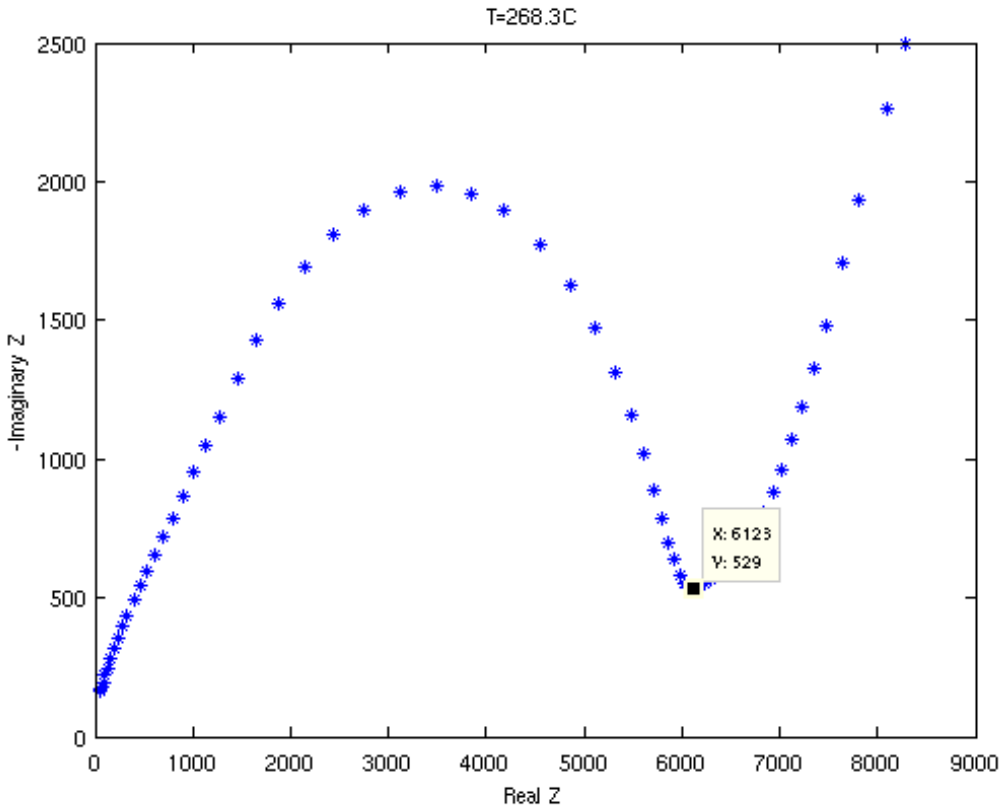

Figure 12: Nyquist plot of sample Red. halfcell measured on 081811 at 268.3^{o}C

The measured data can have many arcs, and for the experiments analysed in this report, at least two separate arcs have been found. These two arcs are said to come from processes in bulk and grain boundary, respectively [34]. For even lower frequencies, electrode effects can also be seen [34]. For the samples analysed during this thesis, it has been quite straightforward to find the resistance of the first arc, by using the procedure mentioned above, however, finding this value for the second arc was a bit more difficult. For the samples analysed here, the needed data had to be extrapolated by fitting a function that gives reasonably good result. During the work it has been found that, if enough of the arc is present, a quadratic function can be used to get results that should not be too far away from the real value. It should be noted however that there is probably a bigger error in the data belonging to the second arc than to the first arc, due to this extrapolation. In figure 13 an example of how this fit can look like. The figure shows the result from measurements done on the sample *Red. half-cell* at 081811, at 723.9^{o}C. In figure 14 the best quadratic function fitted to the data, when up to the last 9 points are removed from the fit, is presented. In the figure to the left the entire set of experiment data can be seen, while the right part is zoomed in on the intersection with the x-axis. From this

picture it can be seen that the deviation resulting from using less points are not that large. The total range from the largest to the smallest value is less than 2% of the mean value. This fact hints that the quadratic fit could be used for these arcs.

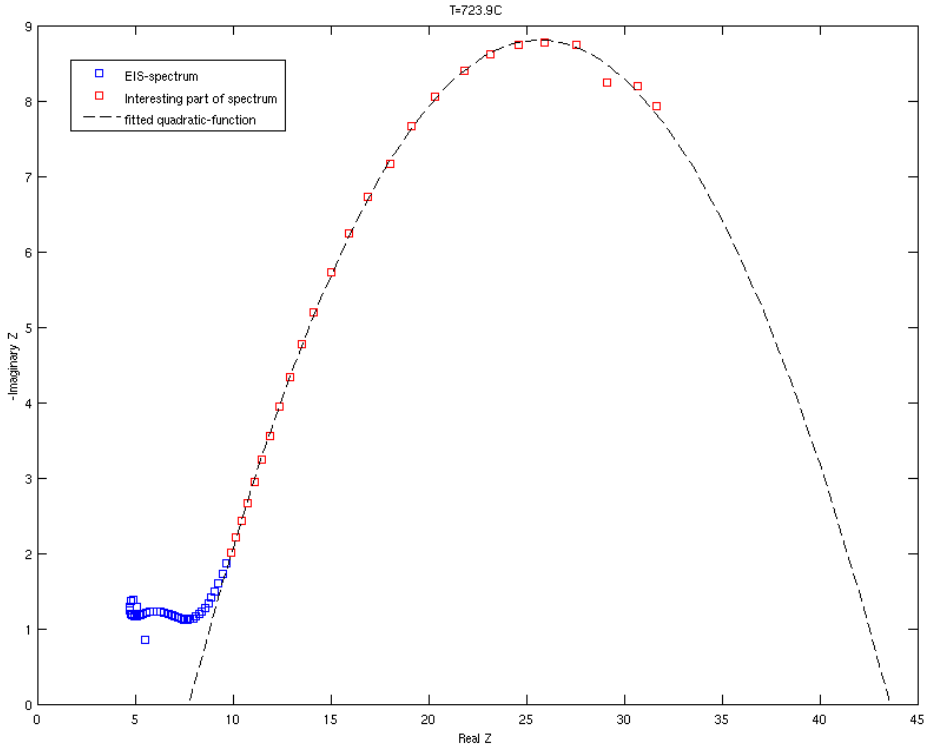

Figure 13: Extrapolating the resistance for the second arc by the use of a fitted quadratic function.

The area in equation (11) was measured when the experiments were conducted, and this is the area of the platinum contact, the thickness can be found from, for example, SEM-pictures, three of them which can be seen in figure 7.

The reason to why the activation energy is the slope of the line resulting from plotting the logarithm of the conductivity against $1/T$ come from the following reasons. The ionic current can, according to the (empirical)Arrhenius equation, be written as: $i = A \exp -E_a/RT$, where A is a constant, E_a is the activation energy, R is the gas constant and T is the temperature in kelvin [35]. Using the conductivity, given by equation (11), and that the resistance can be written as R=U/I, the following linear equation can be derived (12):

$$\log \sigma = -E_a/R \cdot \frac{1}{T} + \log C \tag{12}$$

where C is a constant, T is the temperature in kelvin, E_a is the activation energy and R is the gas constant. For $x = \frac{1}{T}$, $y = \log \sigma$, $m = \log C$ the slope can be written

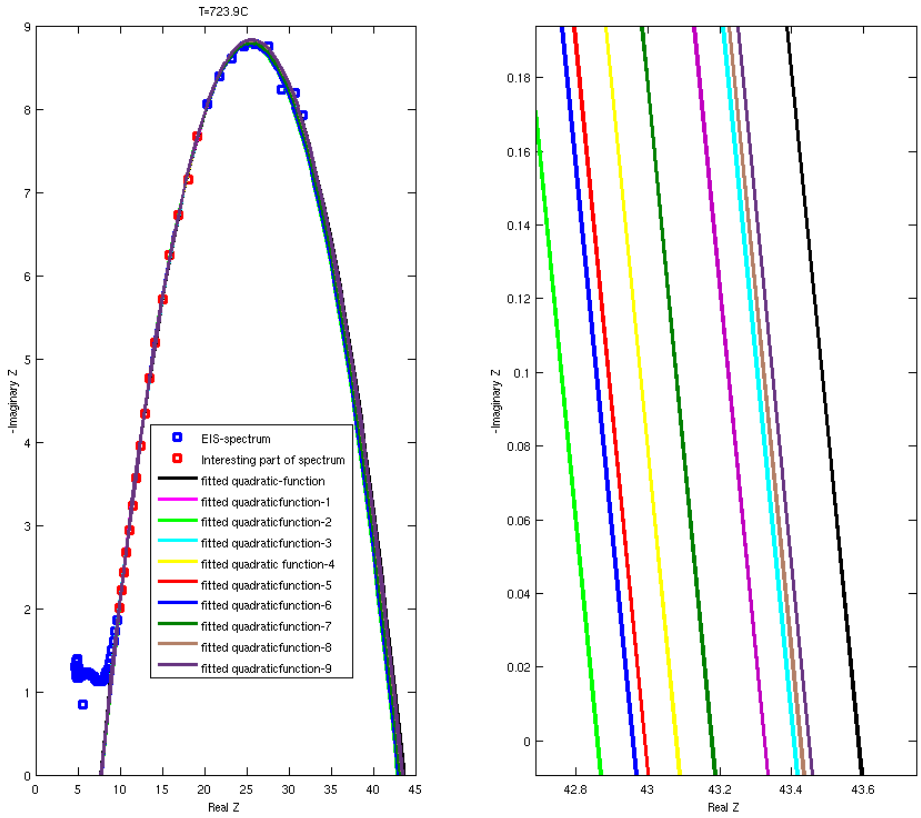

Figure 14: To the left ten different quadratic fits for the second arc, when more and more points are removed, can be seen. To the right, the zoomed in intersection with the x-axis for the ten quadratic fits is displayed.

as $k = -E_a/R$, and thus the activation can be found by finding the slope as for an ordinary linear equation.

4 Results

The results section is divided into two major parts, those related to structural parameters and those related to EIS measurements.

4.1 Structural parameters

In this section the results concerning the structural parameters is presented. The results deal with porosity and TPBs from SEM-pictures and water intrusion measurements.

4.1.1 Porosity

The results from water intrusion measurements and SEM-analysis can be seen in table 3. The Open-porosity was found by water intrusion and the area-porosity was found by the use of the software ImageJ. The dashes that can be seen in the table below, means that the porosity of the sample was neither measured nor approximated. One thing that should be noted here is that the area porosity, actually should give a better value of the porosity of these samples. This is since the samples are laminated(they were laminated in order to increase the weight above 1g in order to decrease the impact of single water drops on the sample) and this lamination seem to lower the porosity.

Table 3: Names and some properties of the samples that were investigated.

Name	**Open-Porosity** [%]	**Area porosity**[%]
Ni/ZrO_2(50/50) 050613	28.6	35
Ni/ZrO_2(50/50) 230513	33.8	43
Ni/ZrO_2(50/50) 220911	19.0	36
Ni/ZrO_2(30/70) 120913	23.0*	26
Ni/ZrO_2(50/50) 180613	25.6	31
Ni/ZrO_2(35/65) 230413	27.3	35
Ni/ZrO_2(50/50) 010414A	-	22
Ni/ZrO_2(50/50) 010414B	-	35
Red. half-cell	-	22
Thin electrolyte	-	20
Not reduced	-	19

In table 3 the * means that the value was not measured with the water intrusion method, but approximated.

4.1.2 SEM-images

In this section the results from the SEM-pictures will be presented. Area porosity that was presented late in the previous chapter is from SEM-pictures as well, but was presented there since it made more sense.

4.1.2.1 Measured results The results that can be seen in table 4 were found from the inspection of the SEM-pictures. In the table, TPB/C means triple-phase-boundary-points on circumference per μm, TPB/A means triple-phase-boundary-points/area per μm^2. The area porosity in table 3 and the $A_{\mathbf{pores}}/A_{\mathbf{total}}$ viewed in table 4 are representing the same quantity, but for different sections. The area porosity is a measure for the whole sample, while the latter is for only the investigated cross-section of the sample. *Red. halfcell* in this table is the sample that corresponds to the samples named 060911, 063011, 070111 and 081811 in table 6. The sample *Not reduced* in this table is the SEM-picture for the sample 052011 in table 6. The sample named *Thin electrolyte* on the other hand corresponds to the sample named 012012 in table 6. The reason for this name difference is that the names in the table 3 and 4 is the names corresponding to some special feature of the sample, while those in the table 6 comes from when the EIS-measurements were conducted, notice that for some samples, several EIS-measurements were conducted.

Table 4: Properties that were extrapolated from the SEM-pictures of the samples that were investigated.

Name	**TPB/C** $[\mu m^{-1}]$	**TPB/A** $[\mu m^{-2}]$	$\mathbf{A_{pores}/A_{total}}$ [%]
Ni/ZrO_2(50/50) 050613	0.65	0.089	40
Ni/ZrO_2(50/50) 230513	0.54	0.106	40
Ni/ZrO_2(50/50) 220911	1.05	0.055	40
Ni/ZrO_2(30/70) 120913	0.34	0.052	27
Ni/ZrO_2(50/50) 180613	0.64	0.086	30
Ni/ZrO_2(35/65) 230413	0.44	0.072	29
Ni/ZrO_2(50/50) 010414A	0.45	0.085	25
Ni/ZrO_2(50/50) 010414B	0.51	0.101	36
Red. half-cell	0.36	0.046	22
Thin electrolyte	0.71	0.074	20
Not reduced	0.45	0.067	19

4.1.2.2 Analysis of the measured results The data gained from the SEM-pictures and water intrusion can be interpreted easier if the results are plotted. Sometimes a property has been plotted against TPB per area and sometimes a property has been plotted against TPB per circumference. This is done because there should not be a strong relationship between the amount of TPB per circumference and porosity. TPB per area is, in contrast to TPB per circumference, dependent on

the porosity of the sample.

In figure 15 the relationship for area porosity vs TPB per area and open porosity vs TPB per area are displayed. These two figures show that there seem to be an increase of TPBs per area when the porosity is increased, at least in the region of porosity that has been investigated here, i.e. around 20% to 40%. The linear fits in the two graphs are there to make the trend more apparent. The slope is about three times steeper in the figure to the right than in the one to the left, suggesting that a change in open porosity has a larger influence than area porosity.

In the article "Quantitative analysis of microstructure and its related electrical property of SOFC anode, Ni-YSZ cermet" by Lee *et al* [8] they report that 40% is the optimal porosity with respect to performance of SOFCs. The amount of TPBs is not the only thing that affect the performance, as mentioned in the theory section properties regarding the transport of gas as well as electronic and ionic conduction in the cell are also important factors.

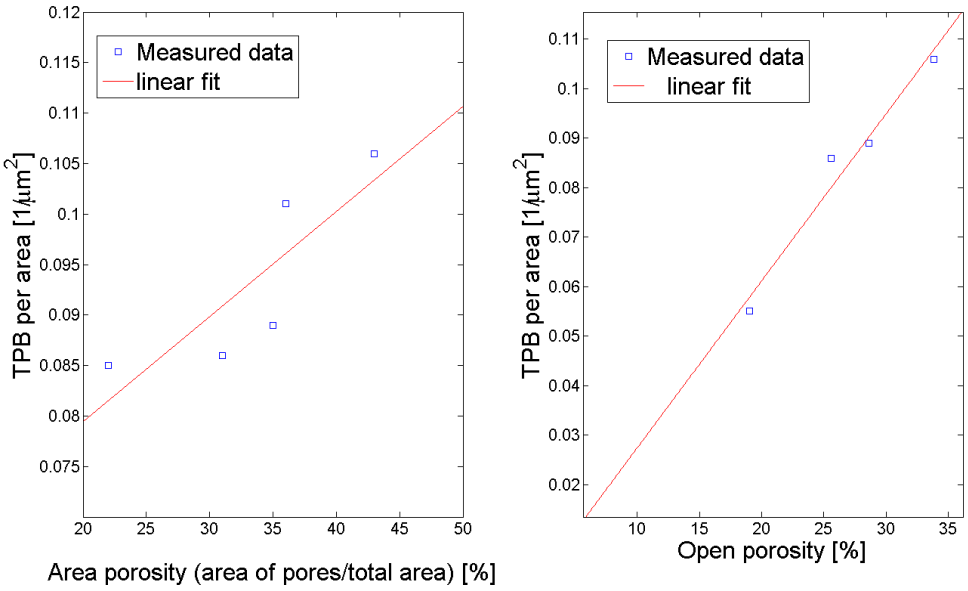

Figure 15: The left plot show the relationship between area porosity and TPB per area. The plot to the right displays the relationship between open porosity and TPB per area.

In figure 16 the relationship between percentage of Ni in relation to amount of Ni and YSZ in the anode versus TPB per circumference is plotted. The figure gives a hint that the highest amount could be achieved when there are equal amounts of Ni and YSZ, or that the number of TPBs increases with a higher amount of Ni. The latter of these results would appear quite strange, there should be a maximum at 50%. No samples with more than 50% Ni were however investigated. The percentage of nickel is measured as the amount of Ni/(the amount of Ni and YSZ combined).

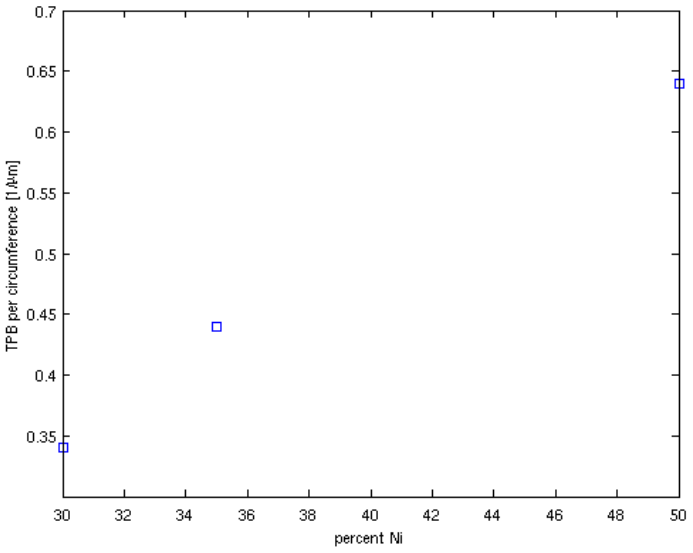

Figure 16: Relationship between content of nickel and TPB per μm on the circumference.

Another exciting property that could be investigated is how the area porosity is dependent on the amount of corn starch. This relationship is presented in figure 17. As expected, the figure suggests that an increased amount of starch gives a higher area porosity. In the figure it can also be seen that the fitted line deviates very little from the black dashed line, that has the equation $y = x$. This means that if 30% corn starch is used in the sample one can expect a porosity of about 30%. However, it can also be seen that there are quite big variations from this line for single samples, up to about 5 percentage points.

In figure 18 it can be seen that an increased amount of TPB on the circumference seem to lead to an increased amount of TPB per area.

In figure 19, the relation between the size of the zirconia particles and the amount of TPB per circumference is plotted. The black squares stem from the first round of samples, the green squares come from the second round. The red line is fitted to the first round of samples, while the blue line is fitted to all of the samples. After the first round the data suggested that the particle size of zirconia have a significant impact on the TPB per μm on the circumference. Verifying this was the major reason for designing this second set of samples in this particular way. From the look of this graph this theory does not look promising, but more and different experiments should be conducted to really investigate the matter. Especially when having the results from Suzuki *et al.* [9] in consideration.

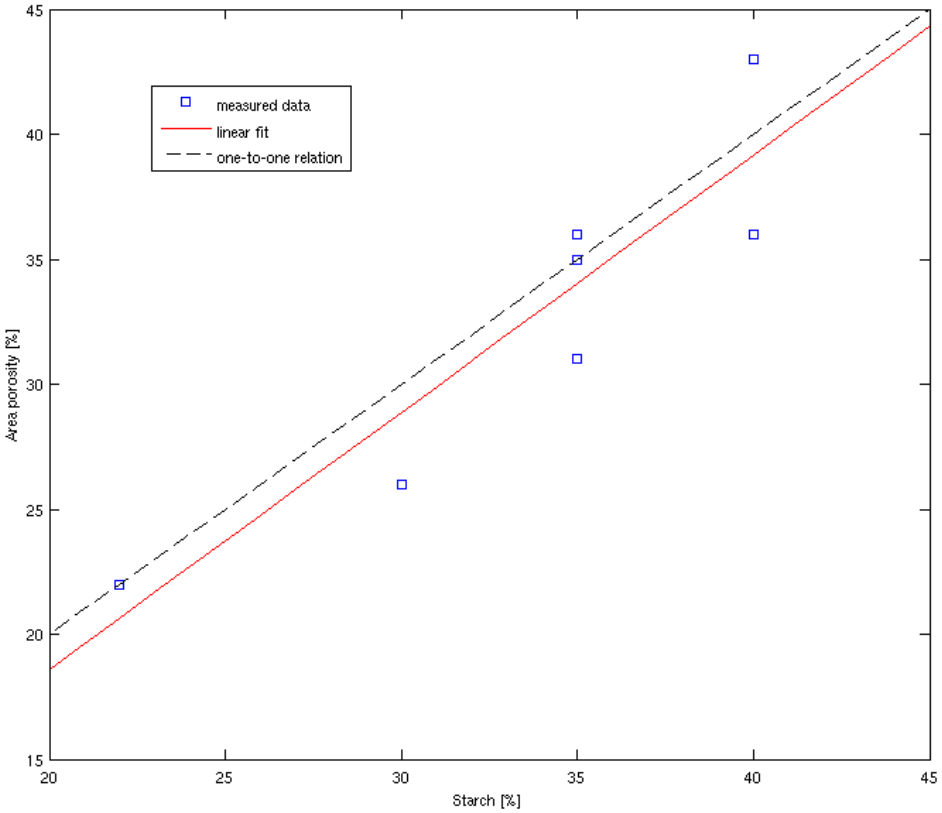

Figure 17: Measured relation between percentage of corn starch and area porosity plotted together with a fitted straight line(red) and the y=x curve(dashed).

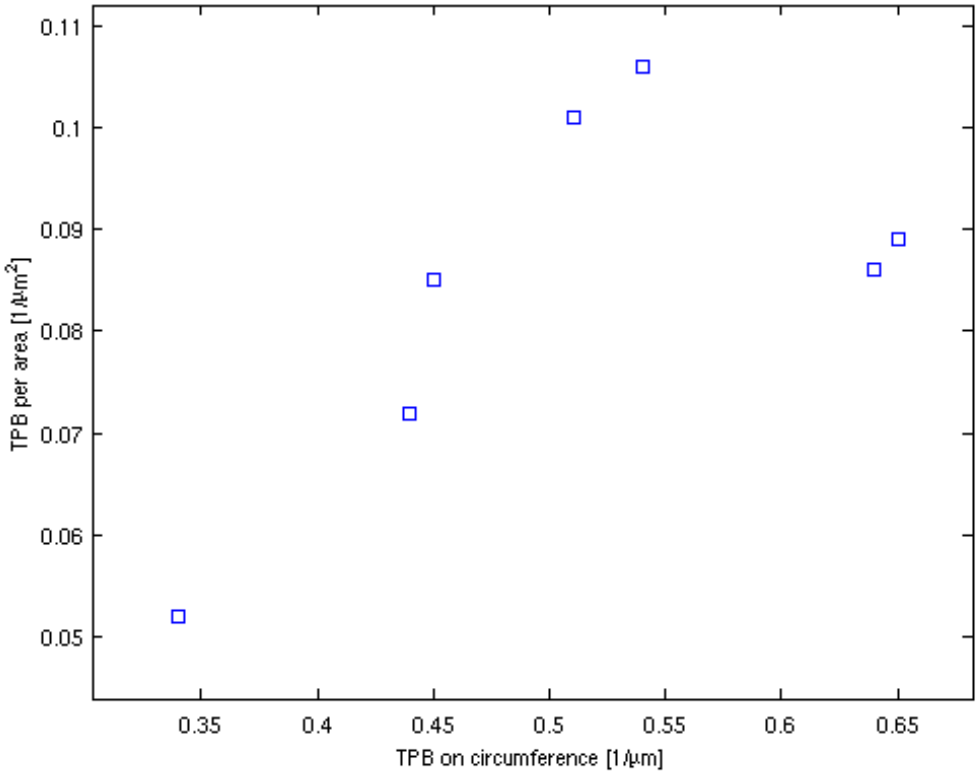

Figure 18: Measurements that show how the TPB per μm on the circumference against TPB per area are related.

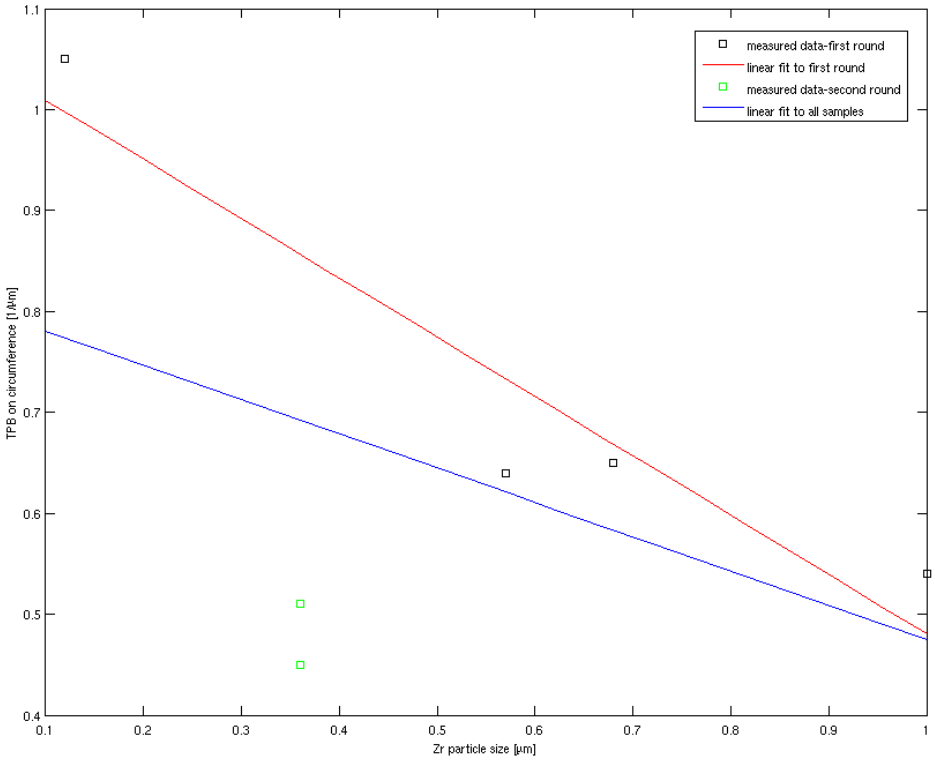

Figure 19: The zirconia particle size plotted against TPB per μm on the circumference. Two different linear fits

4.2 Electrochemical Impedance Spectroscopy

The values that has been choosen as thickness and area for the calculation of conductivity in the different cases can be seen in table 5. Neither the area nor the thickness change the slope of the curves(since they are constants with respect to temperature) only the height of the curve is changed, thus the activation energy is independent of these values, but the conductivity changes with the values. The reason for using different thickness for the different arcs was that some of the results indicated that the arcs came from physical phenomena in electrolyte and anode(see later parts). So choosing the values for the thickness in this particular way can be seen as an experiment, and all results regarding conductivity should be analysed with this in mind.

Table 5: Thickness of the samples and the area of the platinum contacts, used as area, A, and thickness, l, in equation (11).

Sample	**Date**	**Area** $[m^2]$	**1st(electrolyte)** $[\mu m]$	**2nd(anode)** $[\mu m]$
Not reduced	052011	$1.4 \cdot 10^{-4}$	28	270
Red. half-cell	060911	$2.5 \cdot 10^{-5}$	30	300
Red. half-cell	063011	$2.5 \cdot 10^{-5}$	30	300
Red. half-cell	070111	$2.5 \cdot 10^{-5}$	30	300
Red. half-cell	081811	$2.5 \cdot 10^{-5}$	30	300
Thick electrolyte	120811	$2.8 \cdot 10^{-5}$	46	300
Thick electrolyte	121611	$2.8 \cdot 10^{-5}$	46	300
Thin electrolyte	012012	$5.2 \cdot 10^{-5}$	27	100

From the EIS measurements, the activation energy was calculated for the two arcs for the different samples. The $\log \sigma$ vs $1/T$ for the samples named 060911, 063011, 012012 and 121611 can be seen in figures 20-23, in these figures a fitted line can be seen, and as mentioned in the description of the method, the activation energy can be found from the slope of this line. The calculated activation energy, in eV, for the different arcs and samples can be seen in table 6. In this table, the three dashes means that no value could be extracted for these cases. There were different reasons for this. In the case of sample 120811 only one temperature was measured, since the oven was broken during this experiment, and hence no plot of how $\log \sigma$ vs $1/T$ could be created. In the case of the sample measured at 052011, the second arc could not be fitted in the same way as the others. In this case the second arc started to rise instead of going towards the x-axis as in the other cases. The difference can be seen in figure 24, where this odd behaviour can be seen in the figure marked with an A.

If all these straight lines are plotted in the same figure, it is quite easy to see which sample got the best conductivity in different temperature regions. This has been done for the two arcs for the different samples and can be seen in figure 25 and 26. When these curves are investigated closer some conclusions can be drawn. For the first arc, the four measurements done on the same sample, named *Red. half-cell*

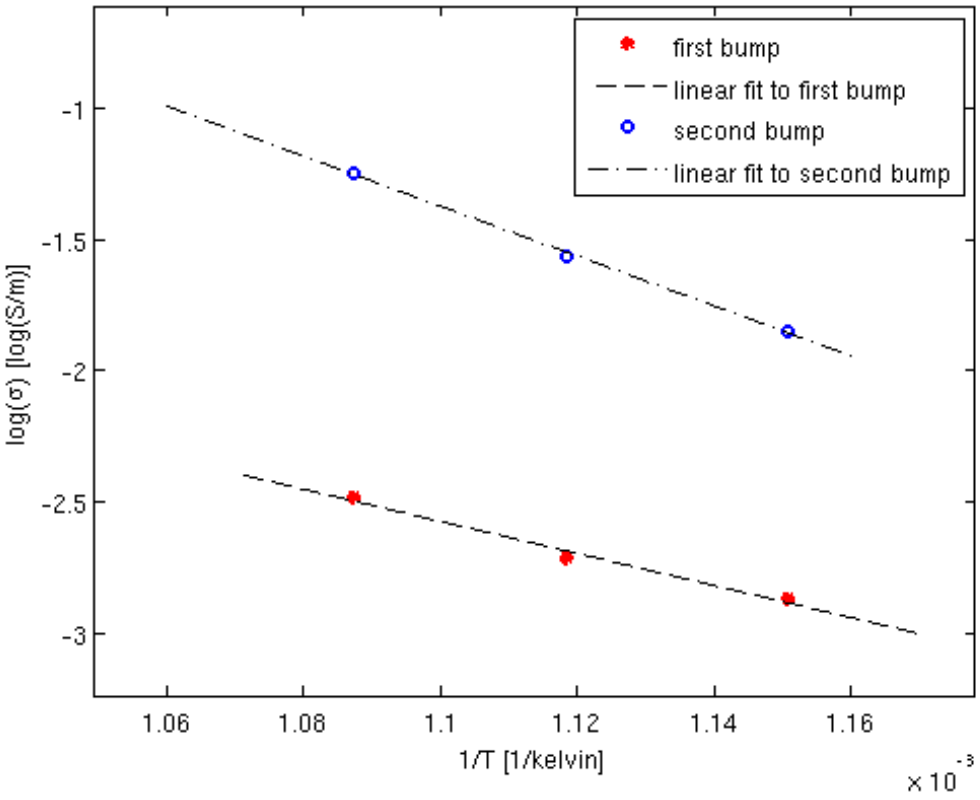

Figure 20: $1/T$ plotted against $\log \sigma$ for the measurements done 060911, with a fitted straight line.

Table 6: Activation energy for the different EIS-measurements for the two arcs.

Sample	**Date**	**First arc** $[eV]$	**Second arc** $[eV]$
Not reduced	052011	1.6790	-
Red. half-cell	060911	0.5250	0.8214
Red. half-cell	063011	0.4777	1.4087
Red. half-cell	070111	0.4724	1.2481
Red. half-cell	081811	0.4668	0.7612
Thick electrolyte	120811	-	-
Thick electrolyte	121611	0.6033	0.8436
Thin electrolyte	012012	0.9401	1.2499

in table 3 and in table 6 and figure 25 named 060911, 063011, 070111 and 081811, have quite similar slope, and therefore activation energy, which can also be seen in table 6, furthermore it can be seen that they are quite close to each other in height, compared to the other samples, which mean that they have similar conductivity as well. If the activation energies are plotted for the different experiments done on sample *Red. half-cell* as in figure 27, it can be seen that the activation energy was lowered after each experiment.

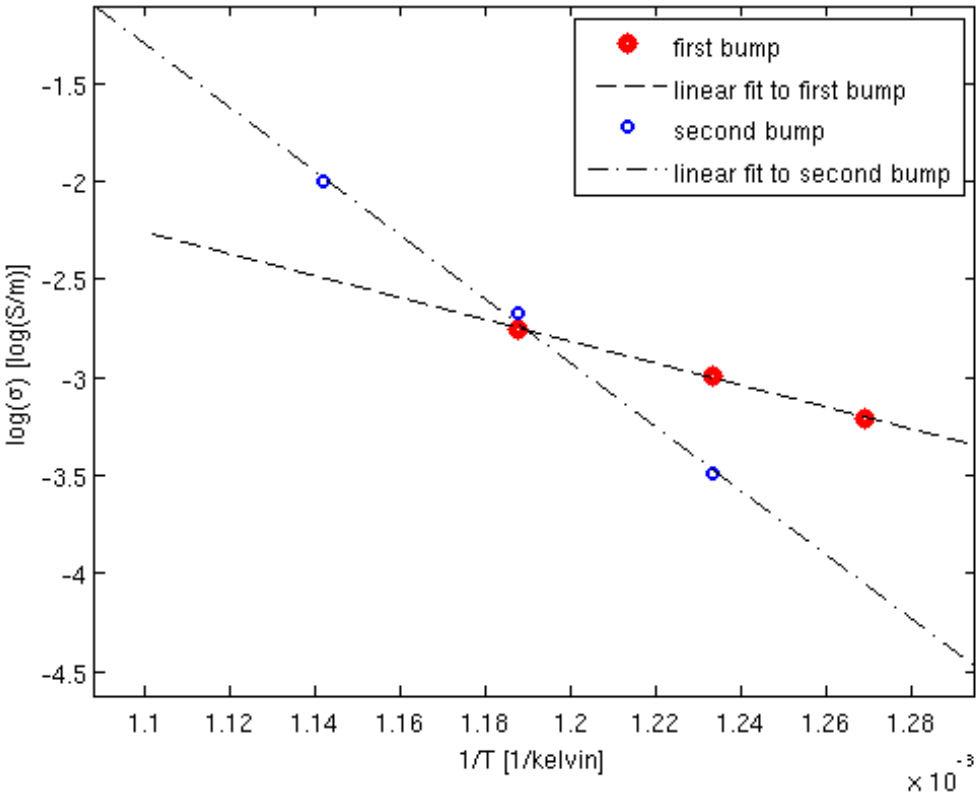

Figure 21: $1/T$ plotted against $\log \sigma$ for the measurements done 063011, with a fitted straight line.

Another result worth pointing out is that the cell named 121611 have approximately the same slope, and thus similar activation energies, this can also be seen in table 6, from the graph however, it can be seen that the sample 121611 have worse conductivity than all those measured for the *red. halfcell*.

When investigating figure 26, and the second arc of the EIS-mesurements, it can be seen that the slopes are not so similar any more for the measurements belonging to sample *red. half-cell*, and thus resulting in different activation energies, which also can be seen being the case in table 6. One interesting aspect is that, if the dates of the experiments are investigated, it can be seen that for the first and last measurement the activation energies are almost equal, but the conductivity is not as good in the latter case. In between these measurements, the activation energy was between 50 and 70% higher. What this change come from is not clear, but could be an interesting phenomena to further investigate. It should however be noted that this phenomena could also be a result from measurement error since an extrapolating technique has been used, and also only quite few points have been used in the linear interpolation.

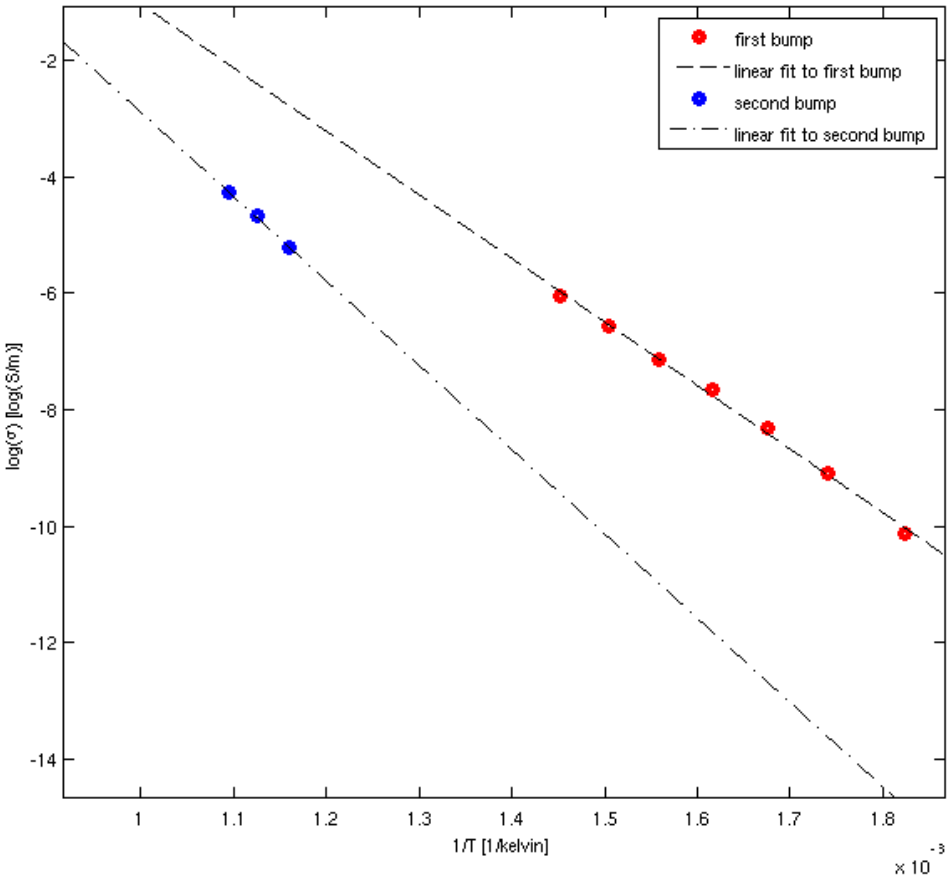

Figure 22: $1/T$ plotted against $\log \sigma$ for the measurements done 012012, with a fitted straight line.

Another thing that is interesting with the sample *Red. half-cell* is that it could be seen afterwards that the electrolyte layer was broken, an SEM-picture of the halfcell can be seen in figure 28. Based on the data from the measurements this probably happened during the last measurement at one of the last temperatures. This conclusion can be drawn since if figure 29 is studied, it can be seen that the last measurement (done at 774°C) does look very strange in comparison to all the others in this figure, notice that both the scale and the shape for the three preceding temperature measurements are substantially different from the one measured at 774°C.

The evolvement of the impedance spectrum can be seen in figure 30. This figure shows the evolvement of sample 110630 for low temperatures. It can be seen that the spectrum has approximately the same shape, but is shrunk as the temperature rises. The shrinking behaviour comes from the fact that the conductivity increases with temperature, which can be seen in figure 25. The same behaviour can be seen in figure 31 for sample 110818, but in a higher temperature region.

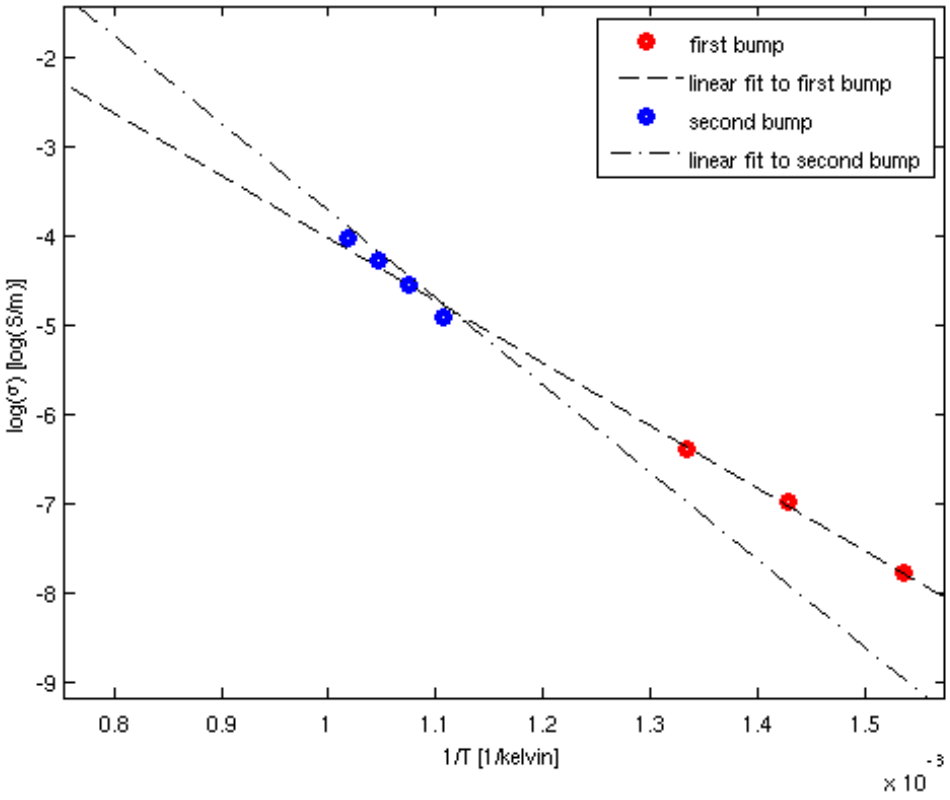

Figure 23: $1/T$ plotted against $\log \sigma$ for the measurements done 121611, with a fitted straight line.

How the different Nyquist plots differed from each other can be seen in the four figures 32-35 for some of the samples and temperatures. In figure 32 all samples that have a result in table 6 (except 060911) are displayed for a quite low temperature. Sample 060911 is not displayed in this figure as it was not measured in this tempereature range, as can be seen in table 2. It is hard to see the results for samples 063011, 070111 and 081811 in figure 32. They are located in the bottom left corner, and can be seen in more detail in figure 35.

How these EIS measurements change at higher temperature can be seen in figure 33 and figure 34, for an intermediate and high temperature, respectively. It can in these figures be seen that the impedance is lowered when the temperature is higher.

In figure 35 three diffrent plots can be seen, all showing the results from EIS measurements in the Nyquist way for the cell named *Red. half-cell*. The plot in the top shows measurements for the lowest temperature and then the temperature is higher in the middle one and the temperature is highest in the plot at the bottom. These results are also plotted in the figures 32, 33 & 34 but are quite hard to see.

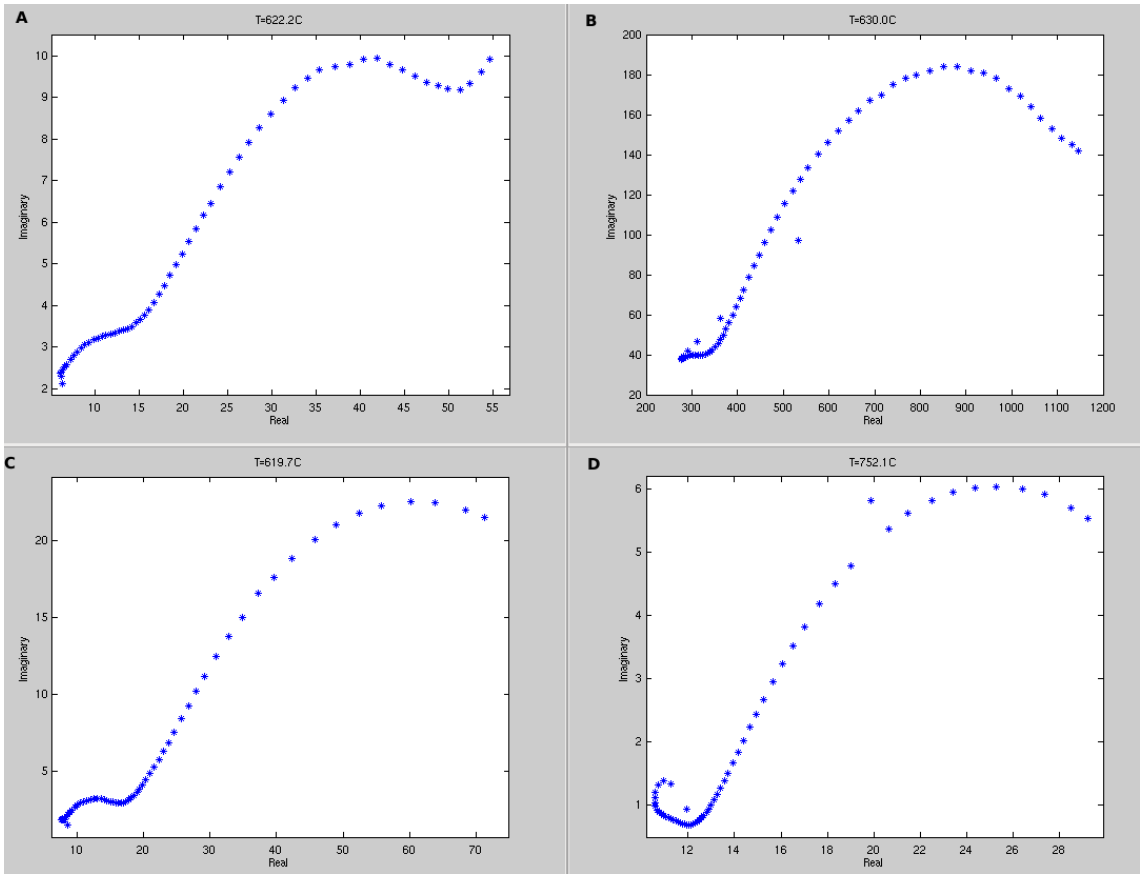

Figure 24: Four different EIS-spectrum at approximately the same temperature for A-C and one at a more elevated temperature. The samples are arranged in the following way: A:052011, B:121611, C:110818 and D:110818.

If tables 2, 4 and 5 are investigated closer it can be seen that sample *Not reduced* and *Red. half-cell* are quite similar, and especially measurement 052011 is very similar to 063011. The difference between the two is that the first sample is not reduced. Figure 36 and figure 37 show the resulting EIS measurements for the sample *Not reduced* for high respectively low temperature. Figure 38 and figure 30 show the resulting EIS measurements for high respectively low temperatures for sample *Red. half-cell* and experiment 063011. If these figures are compared it can be seen that they have different shapes. It can be seen that the first arc at lower temperatures of the samples belonging to *Not reduced* are more round than the sample belonging to *Red. half-cell*. It can also be seen that the curve after the first arc look different in the two cases. For higher temperatures it can be seen that the first arc of the sample belonging to *Not reduced* has almost disappeared, while it can still be seen for sample *Red. half-cell*. As mentioned earlier it can also be seen in the sample *Not reduced* that the curve for the second arc starts to rise again, especially at the absolute highest temperatures, a behaviour that is not seen for the sample *Red. half-cell*. This difference in shapes should come from the fact that the first sample is not reduced while the other is, since this is the only apparent difference between the two.

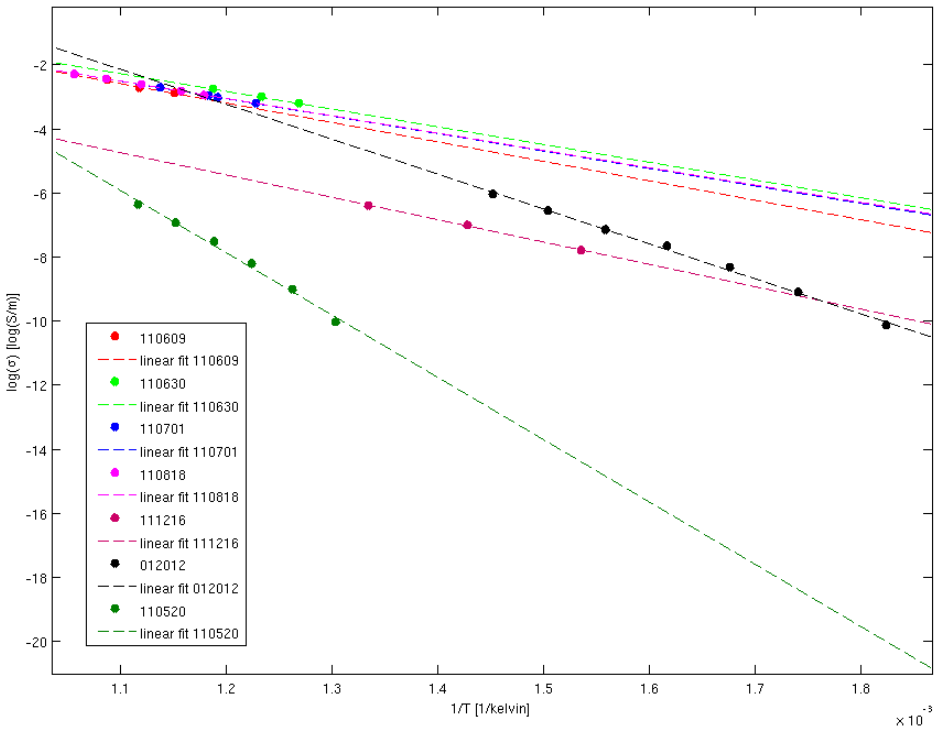

Figure 25: $1/T$ plotted against $\log \sigma$ for the first arc for all measurements, with fitted straight lines.

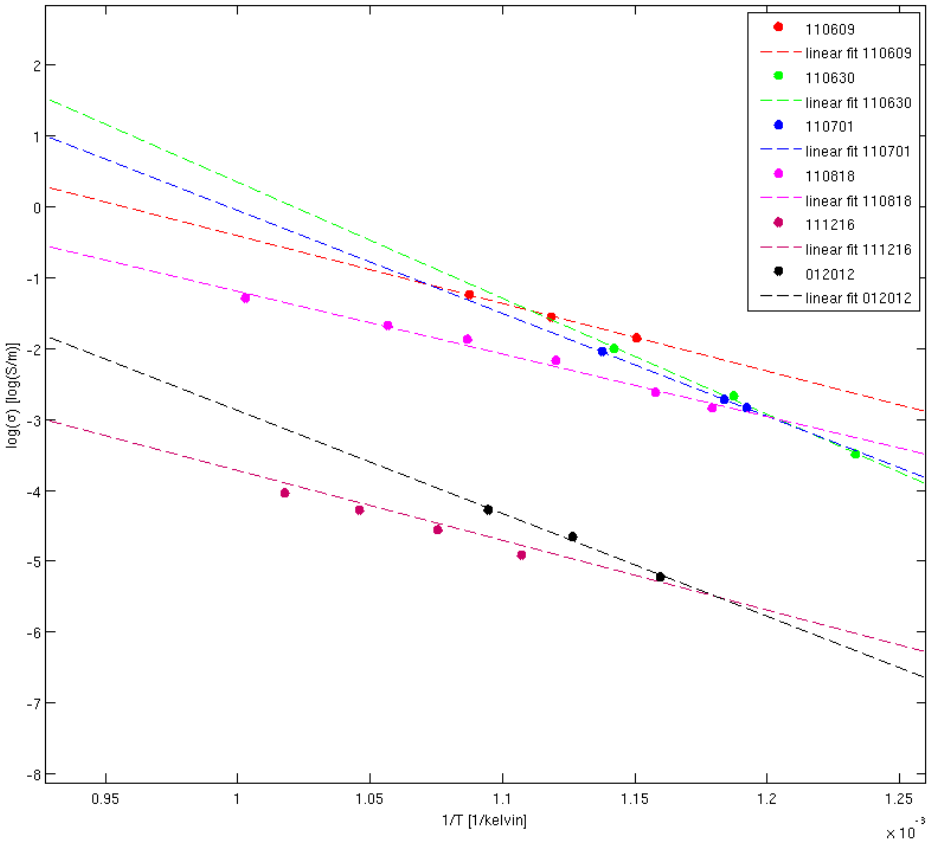

Figure 26: $1/T$ plotted against $\log \sigma$ for the second arc for all measurements, with fitted straight lines.

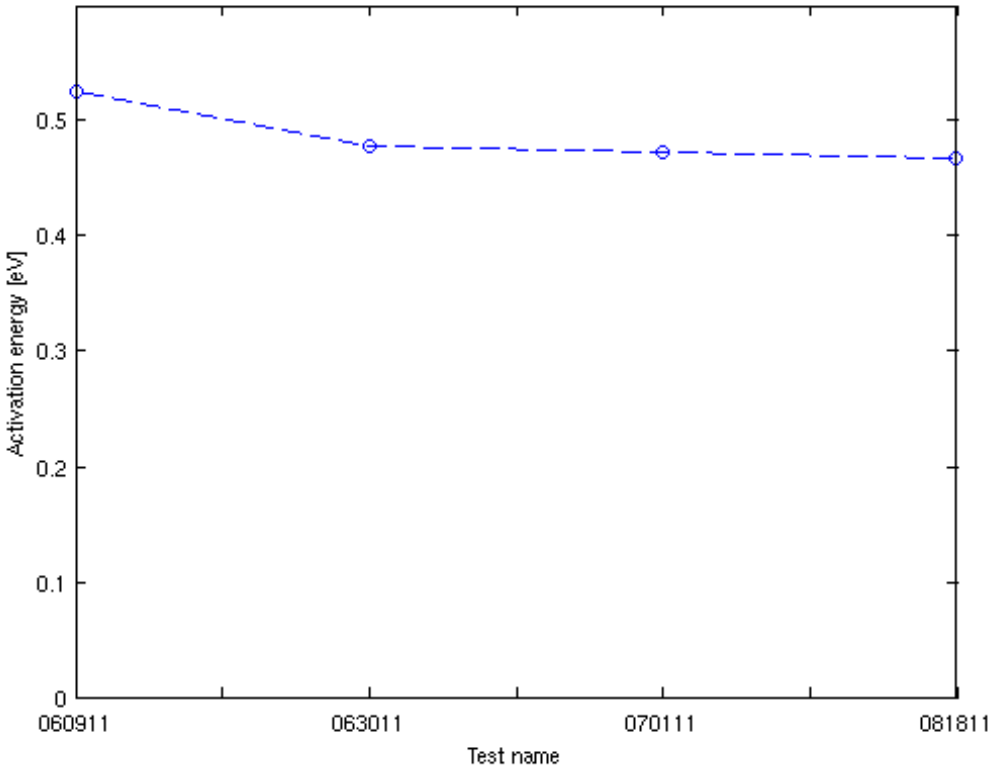

Figure 27: The activation energies for the different EIS measurements on sample *Red. half-cell* plotted against which date they were measured.

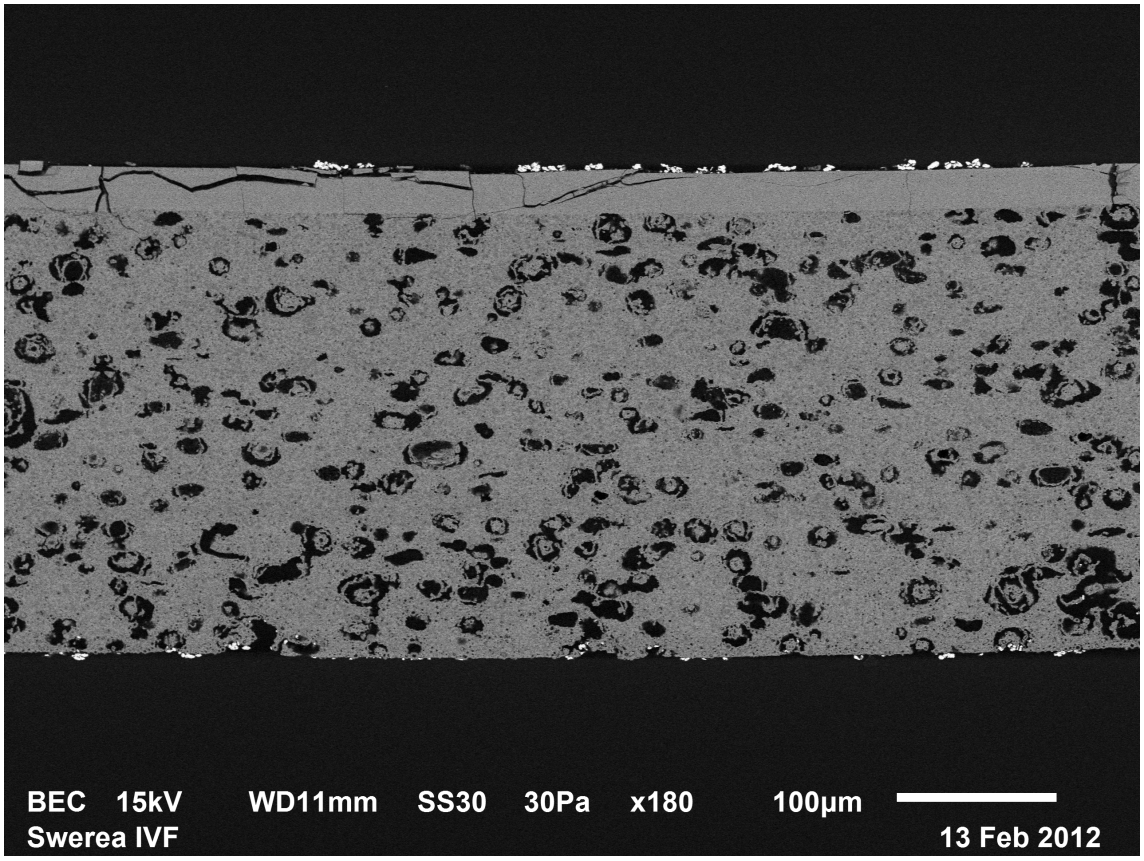

Figure 28: SEM-picture of the half cell named red. halfcell in table 4 that was done after the measurement series called 081811.

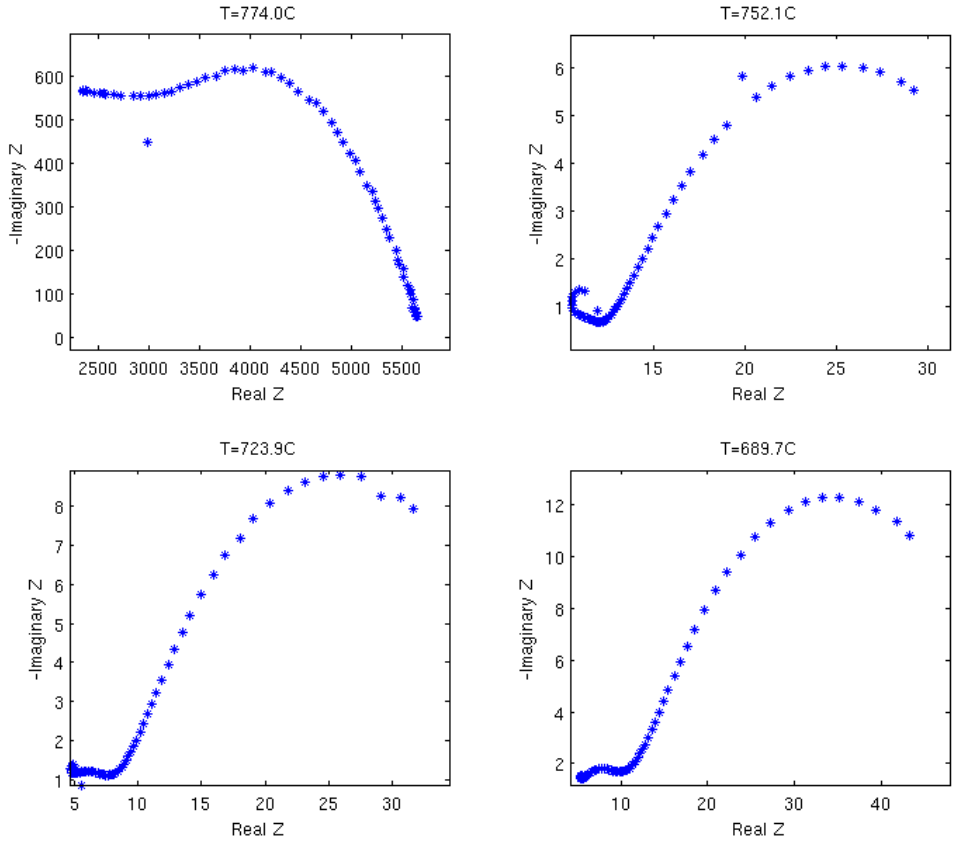

Figure 29: The four last EIS-mesurements for the mesurement-series named 081811.

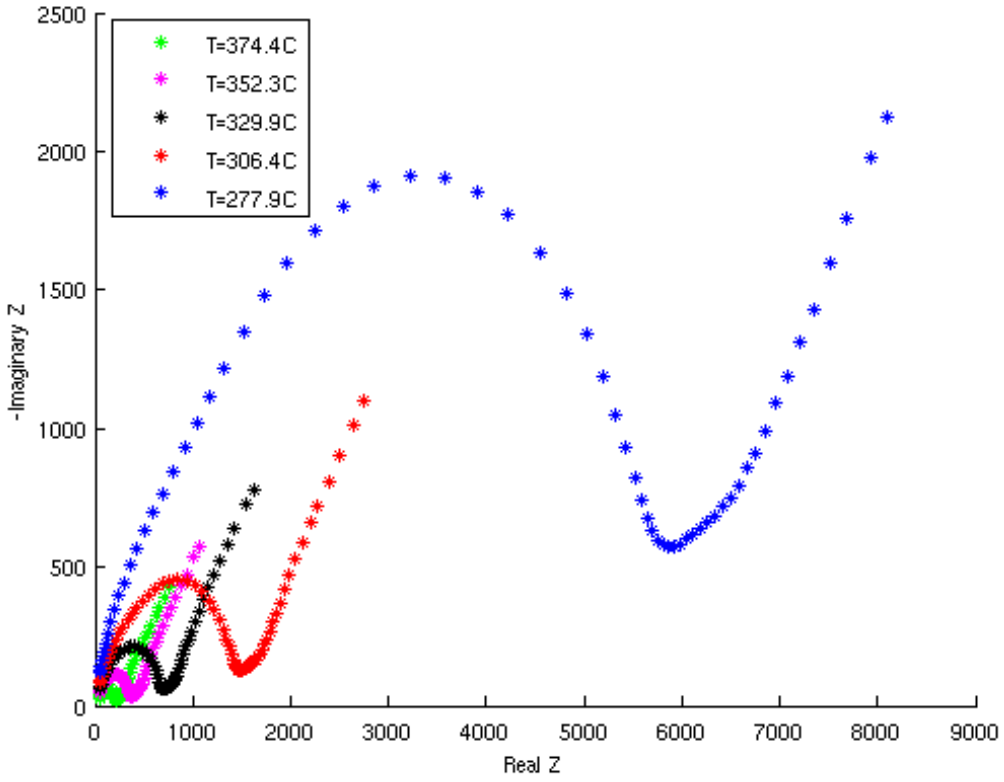

Figure 30: EIS-measurements for the the sample named *Red. halfcell*. The curves show how the impedance changed with temperature for the experiment done at 110630 for low temperature.

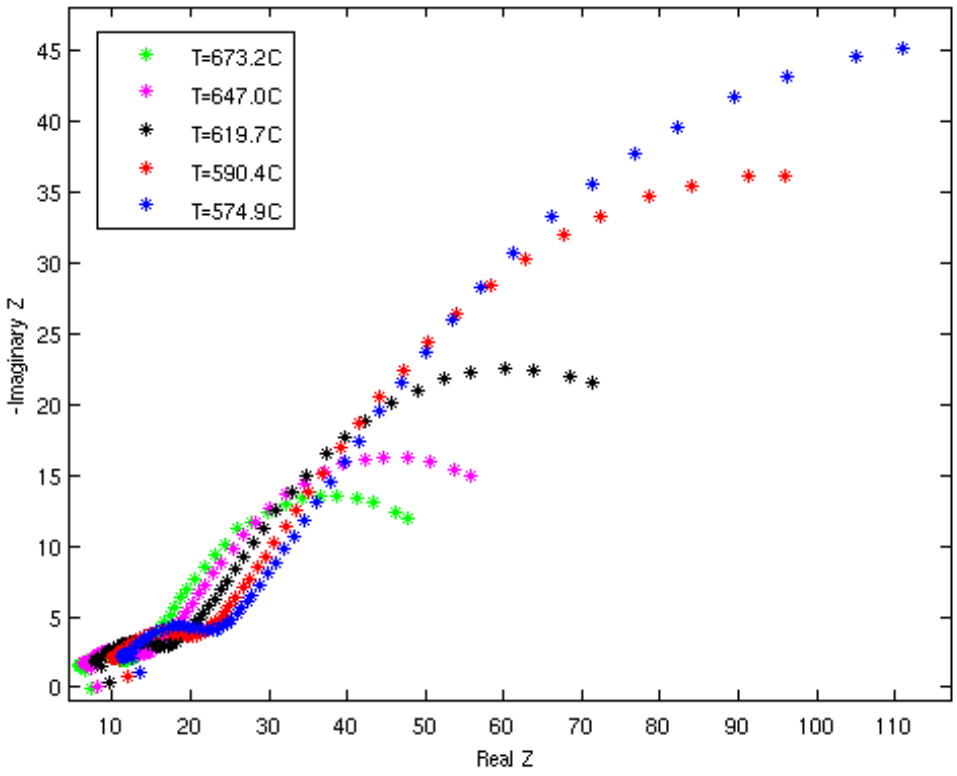

Figure 31: EIS-measurements for the sample named *Red. halfcell*. The curves show how the impedance changed with temperature for the experiment done at 110818 for high temperature.

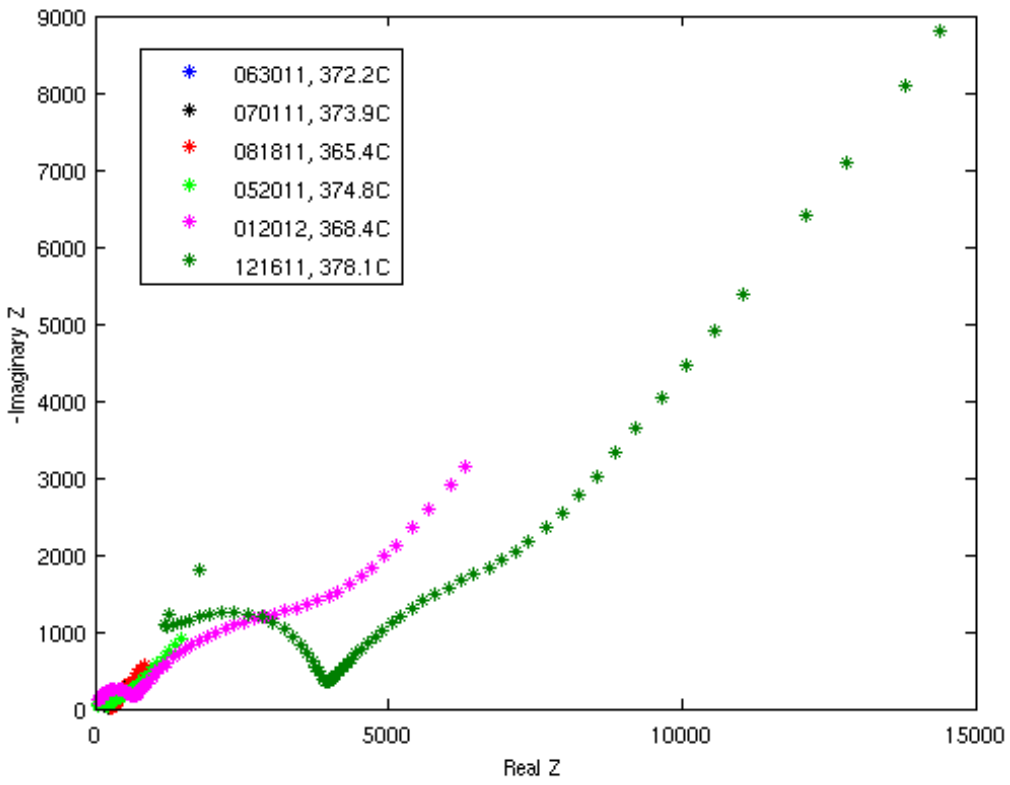

Figure 32: Nyquist plot showing the results from EIS-measurements for six of the different samples at approximately the same temperature. This was one of the lowest temperatures that was measured.

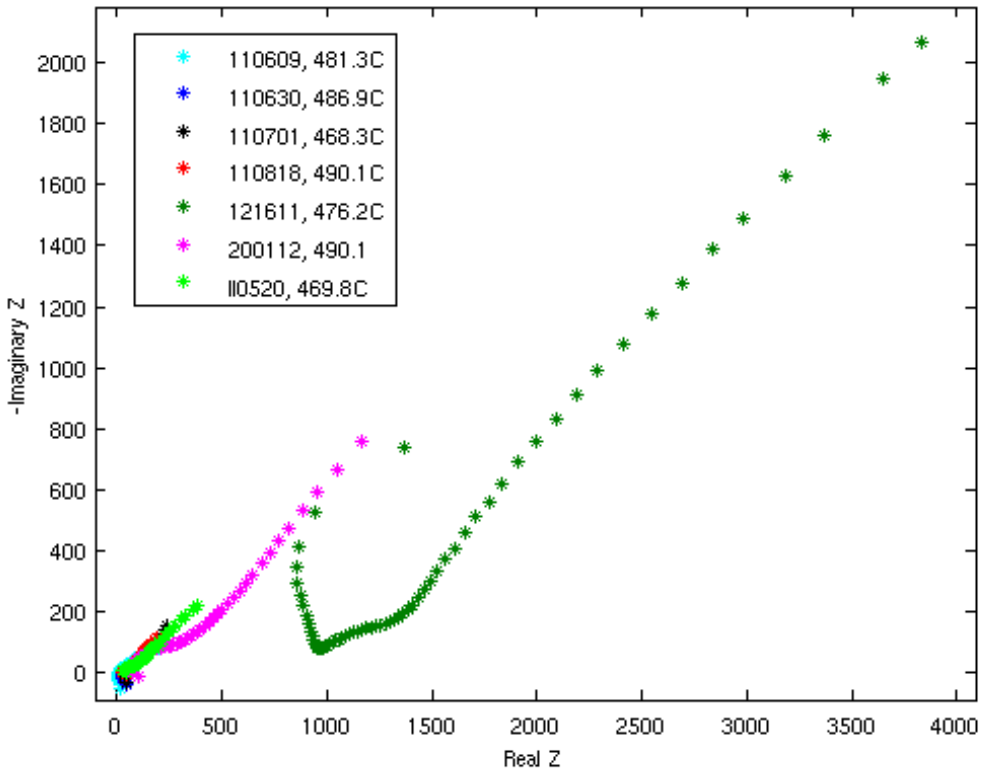

Figure 33: Nyquist plot with the results from EIS-measurements for all seven samples that was analysed at an intermediate temperature. The temperature in all cases are approximately the same.

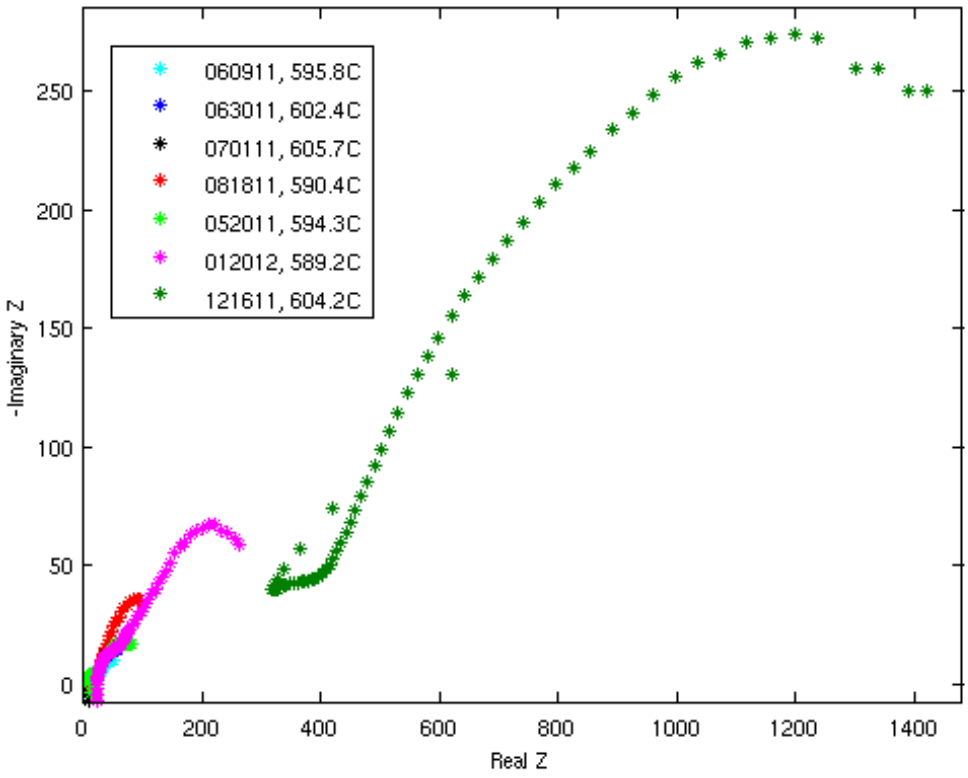

Figure 34: Nyquist plot with the result from seven different EIS-messurements of differenent samples. All these samples have approximately the same temperature and it is also a quite high temperature.

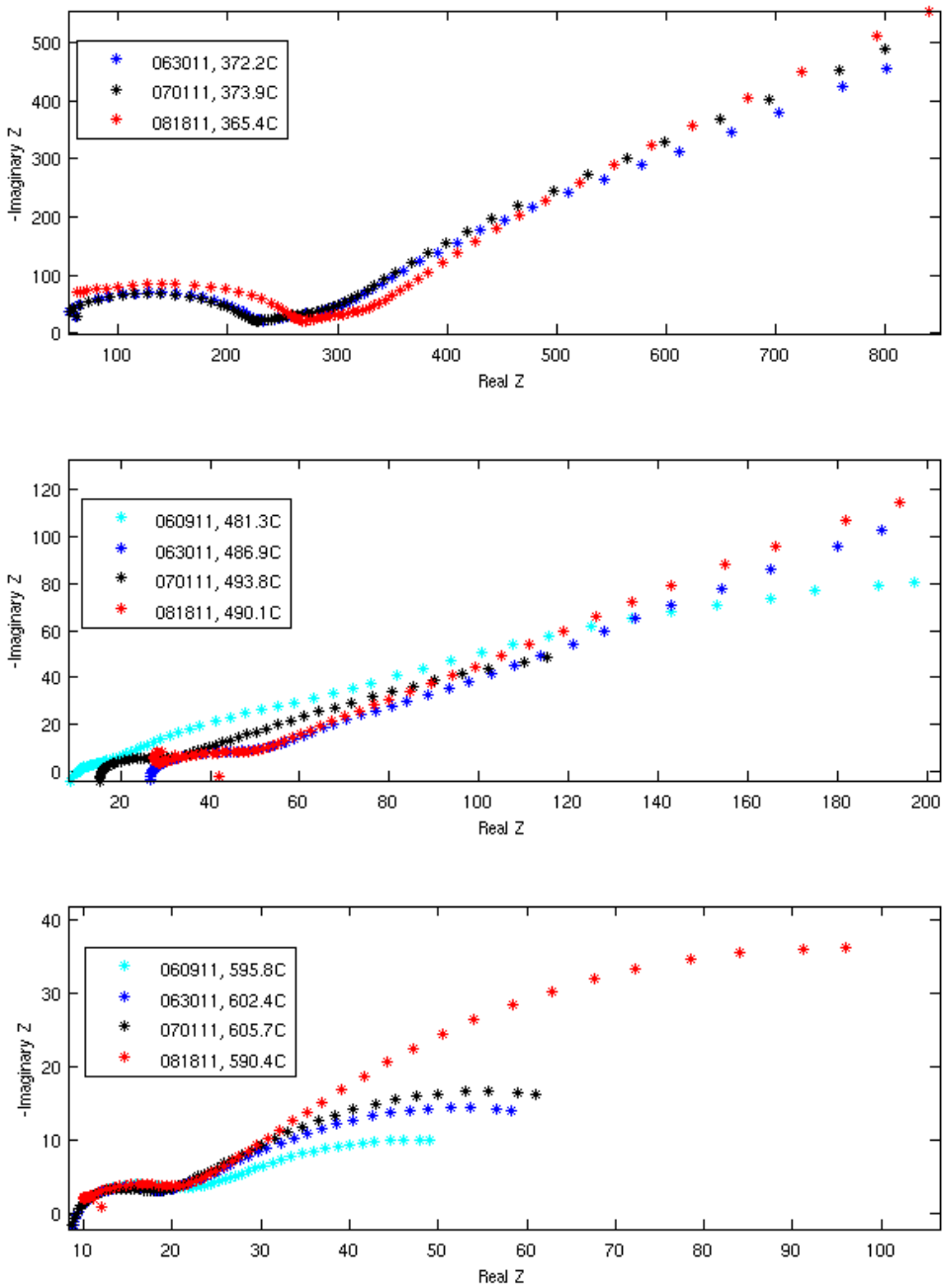

Figure 35: EIS-measurements for the samples belonging to the sample named *Red. halfcell*. They are measured at similar temperatures for low(highest plot), intermediate and high temperature(lowest plot).

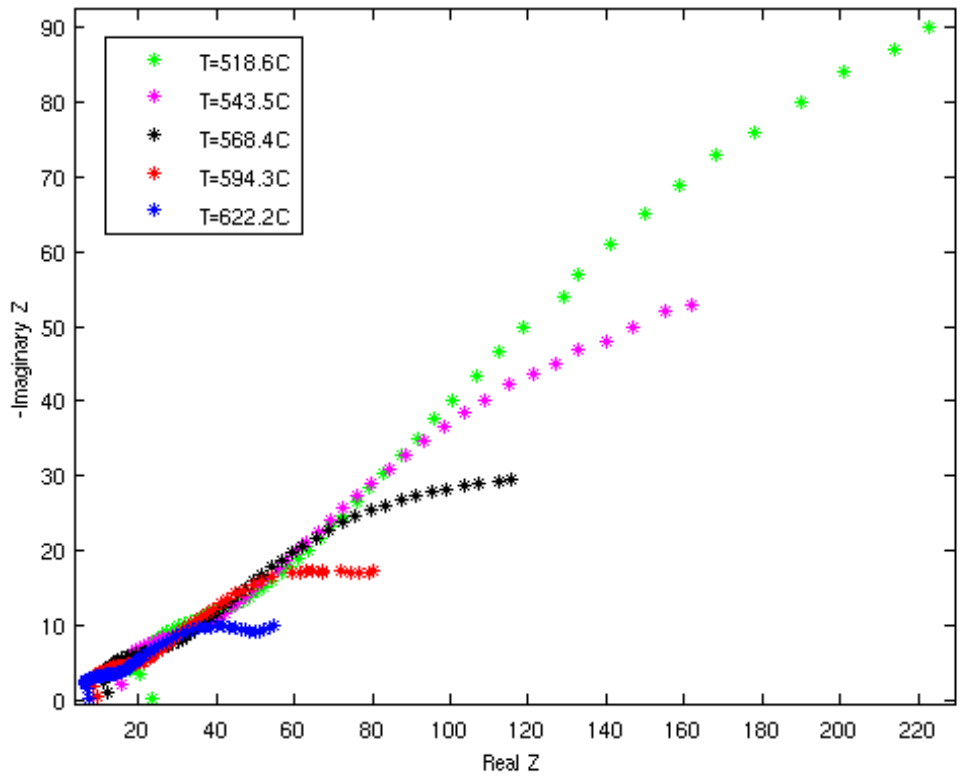

Figure 36: EIS-measurements for the sample *Not reduced* at 052011. They are measured at different high temperatures.

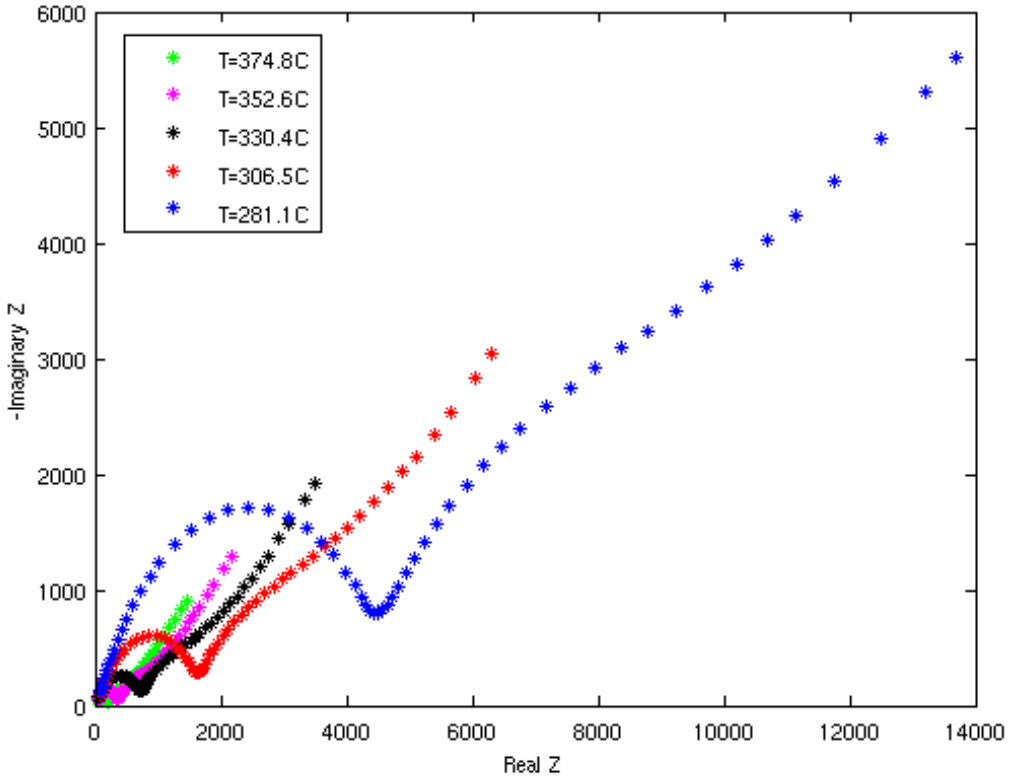

Figure 37: EIS-measurements for the sample *Not reduced* at 052011. They are measured at different low temperatures.

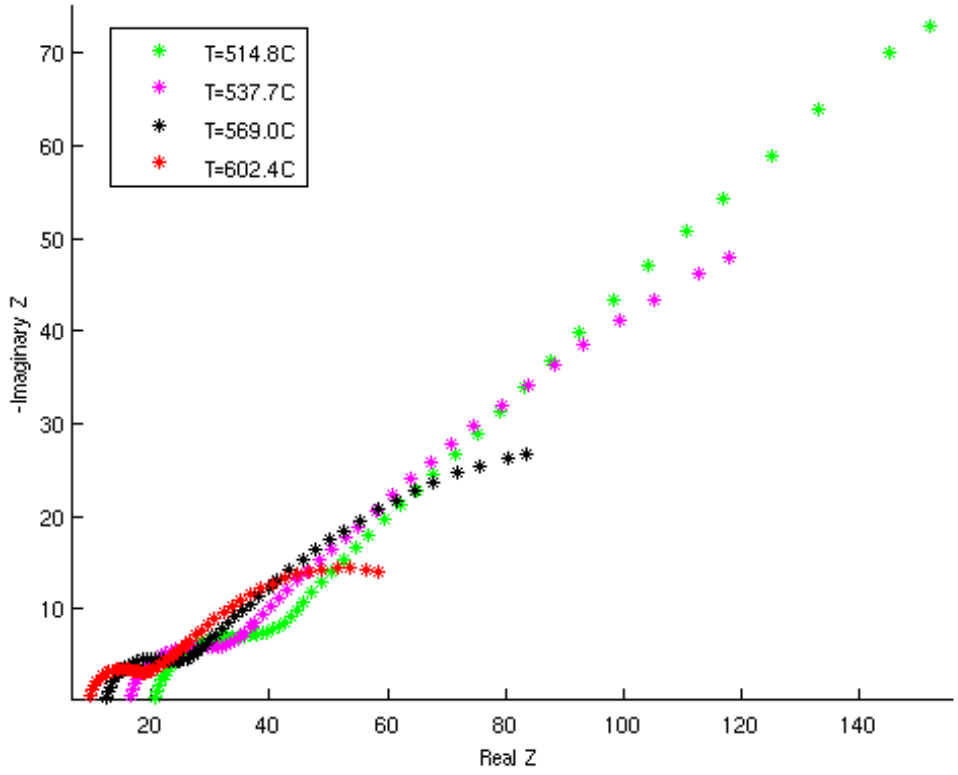

Figure 38: EIS-measurements for the sample *Red half-cell* at 063011. They are measured at different high temperatures.

5 Discussion

In this section the most interesting results from the different measurements will be discussed. The discussion is separated in two sections.

5.1 SEM and porosity measurements

Figure 15 suggests that the larger porosity a sample got, the greater amount of TPB per area will the sample have, at least in the region 20-40%. It has been reported by others that the highest performance of an SOFC is for an open porosity of about 40%. It is not certain that, if a sample is produced with a porosity higher than 40%, this trend will stop. It is not only the amount of TPBs that is responsible for the performance, but also, for example, the ability for the gases to flow as well as the electronic and ionic conductivity of the cell. All these other properties are also dependent on the porosity. These properties' impact on the performance have not been investigated in my work, except for literature studies. Two things that have a big impact on the TPB per area is the circumference and the TPB per circumference. If the total circumference of the pores is increased with a higher porosity, then an increased TPB per area is probable to be observed as well. Though, it is probably not possible to produce a sample with much higher porosity than 40% that can be used practically, since it was observed that already at 40% the sample had visible cracks.

If figure 17 is investigated more thoroughly it can be seen that if x volume-% of starch is added to the anode, the anode will get a porosity close to x%. Furthermore, the result of the measured porosity of the anode gives a hint that this porosity deviates more from this expected value when more starch is added to the mix. To be able to draw this conclusion with higher certainty, more measurements would be required. This conclusion would however appear logical, since it could be expected that an error in the volume percentage of starch could be larger the more starch there is in the sample.

One aspect that need to be pointed out and discussed is the fact that the measured point in the upper left corner in figure 19 comes from a sample where potato starch was used instead of corn starch. This point has a big impact on the look of the fitted line. Since the TPB on circumference has been used in this plot, the pores should have approximately the same shape in order to give reasonable result. If the SEM-pictures in figure 6 are compared, it can be seen that the pores belonging to the one with potato starch(marked with a C) in the figure has different looking pores than the corn starch(the rest of the samples). This fact combined with the last two (green) measurements make the plausability, that the particle size of zirconia is a factor that has a big impact on the amount of TPB, quite small. The theory should not be rejected completely, but instead there should be conducted similar measurements to the ones done by Suzuki *et al.* [9]. If the Ni particles can make the microstructure better so could possibly also the zirconia particles do.

5.2 EIS-measurements

The fact that the second arc of sample 052011 cannot be fitted in the same way as the others(see difference in figure 24) suggest that there is something different with this sample. Indeed, this sample is the only sample that was not reduced prior to the EIS-measurements. This means that the NiO has not been reduced to Ni in the anode. This could be the reason for the odd looking second arc of this sample. This was the most important result that could suggest that the second arc come from something that happens in the anode, and the reason for trying these different thicknesses for the first and second arc. Since this result was only seen in one single sample, it is too bold to draw the conclusion that this actually is the case from these measurements. To verify this, more samples should be analysed. The best would probably be to analyse the same sample, first as not reduced and then reduce it and do the same measurements again.

In table 6 it can be seen that the activation energy is decreasing for each measurement on the sample Red. half-cell. This could parhaps be explained by the fact that as the experiments are done the sample is changed in a way to lower the activation energy. This result suggest that some change in the sample is happening during or in between the measurements. It should be noted here, as can also be seen in the table 2, that the temperature is quite high, and perhaps this change of temperature could stimulate a change. Because sample *Red. half-cell* broke after measurement 081811, no further measurements could be done on this sample. This was a bit unfortunate since it would have been intersting to see if the behaviour would continue to change when the measurements were done again. It would also be interesting to see if the activation energy would continue to be lowered if the measurements were done more times, and perhaps converge to some value. If more experiments would have been conducted on this sample, there is a possibility that these results would contradict this theory. If figures 25 and 26 are studied in more detail, it can be seen that quite a few of the linear fits are done for less than four points, which mean that errors could change these results quite much.

It can be seen in figure 32, figure 33 and figure 34, that the sample 121611 is substantially different from the other ones when it comes to value of impedance. In figure 32, for example, the first minimum is almost at 5000Ω, while the others are below or around 1000Ω. The only big difference between this and the other samples that are not reduced is that it has an approximately 50% thicker electrolyte. This could lead to a higher impedance. This could also explain why this sample does not have a very high activation energy even though it has such a high impedance; the resistivity changes with temperature in the same way as the others but the electrolyte has a much higher thickness.

6 Conclusion

The most important result from this work is presented in this section. The section is divided in the same two parts in which the discussion is divided.

6.1 SEM and porosity measurements

The results from this thesis suggest that an increase of porosity lead to an increase of TPBs per area in anode samples, in the porosity region 20-40%. This increase also appear to be quite linear. How the particle size of zirconia impact the amount of TPBs per μm is inconclusive, at least in the range of 0.12-1μm. The results also suggest that there could be a higher deviation in porosity from the expected starch porosity when there is more starch added, but on average it seems to follow a linear relationship close to "porosity of sample"="volume percent of starch added".

It would have been interesting to make real fuel cell measurements on these anodes to be able to draw a few more conclusions. Maybe this could be an interesting future theme of another research project.

6.2 EIS-measurements

Unfortunately, the porosity for the half-cell samples were almost the same, as can be seen in table 3, so no conclusions how the porosity may impact the results from EIS measurements. However, the data from the four EIS-measurements conducted for sample *Red. half-cell* suggest that the activation energy of the cell for the first arc could be decreased as more measurements are conducted. This could also just be a coincidence and be within the margin of errors. The data also suggest that the shape of the Nyquist plots differ from a sample that is reduced and one that is not reduced, with the other major parameters being the same. It was also seen that a thicker electrolyte gave rise to a much higher resistance, but not necessarily a higher activation energy.

For another research project, it would be interesting to conduct EIS measurements on samples with different porosity, to see if any conclusion could be drawn.

References

[1] Boudghene Stambouli, A. & Traversa, E. (2002) Solid oxide fuel cells (SOFCs): a review of an environmentally clean and efficient source of energy. *Renewable and Sustainable Energy Reviews*, volume 6, issue 5, pp. 433-455.

[2] Minh, N. Q.(1993) Ceramic Fuel Cells. *Journal of the American Ceramic Society*, volume 76, issue 3, pp. 563-588.

[3] McIntosh, S. & Raymond, J. (2004) Direct Hydrocarbon Solid Oxide Fuel Cells. *Chemical Reviews*, volume 104, issue 10, pp. 4845-4865.

[4] Li, X. (2006) *Principles of Fuel Cells* New York, New York: Taylor & Francis Group.

[5] Müller, M. (2012) Regenerative Fuel Cells. In *Fuel Cell Science and Engineering; Materials, Processes, Systems and Technology*, ed. D. Stolten and B. Emonts, pp. 219-245. Darnstadt: Wiley-VCH.

[6] Grove, W. R. (1839) On Voltaic Series and the Combination of Gases by Platinum. *Philosophical Magazine*, volume 14, issue 86, pp. 127-130.

[7] Yuan, X.-Z., Song, C., Wang, H. & Zhang, J. (2010) *Electrochemical Impedance Spectroscopy in PEM Fuel Cells-Fundamentals and Applications*. London:Springer.

[8] Lee, J.-H., Moon, H., Lee, H.-W., Kim, J., Kim, J.-D. & Yoon, K.-H. (2002) Quantitative analysis of microstructure and its related electrical property of SOFC anode, Ni-YSZ cermet. *Solid State Ionics*, volume 148, issue 1, pp. 15-26.

[9] Suzuki, T., Hasan, Z., Funahashi, Y., Yamaguchi, T., Fujishiro, Y. & Awano, M. (2009) Impact of Anode Microstructure on Solid Oxide Fuel Cells. *Science*, volume 325, issue 5942, pp. 852-855.

[10] Kong, J., Sun, D., Zhou, N., Mu, J. & Qiao, J. (2007) Ni-YSZ gradient for anode-supported SOFCs. *Journal of Power Sources*, volume 166, issue 2, pp. 337-342.

[11] Larmine, J. & Dicks, A. (2003) *Fuel cell systems explained*. [Electronic] 2nd edition. Chichester: John Wiley & Sons Ltd.

[12] Hussain, M. M., Li, X & Dincer, I. (2006) Mathematical modeling of transport phenomena in porous SOFC anodes. *International Journal of Thermal Sciences*, volume 46, issue 1, pp. 48-56.

[13] Clarke, S. H., Dicks, A. L., Pointon, K., Smith, T. A. & Swann, A. (1997) Catalytic aspects of the steam reforming of hydrocarbons in internal reforming fuel cells. *Catalysis Today*, volume 38, issue 4, pp. 411-423.

[14] Torabi, A., Etsell, H. T. & Sarkar, P. (2011) Dip coating fabrication process for micro-tubular SOFCs. *Solid State Ionics*, volume 192, issue 1, pp. 372-375.

[15] Topsoe Fuel Cell (2014) Cell production. *Topsoe Fuel Cell*. www.topsoefuelcell.com/products/production/cell_production.aspx. (2014-06-09)

[16] Roosen, A. (2012) Tape casting. In *Ceramics Science and Technology*, ed. R. Riedel and I-W. Chen, pp. 39-58. Darmstadt: Wiley-VCH Verlag GmbH & Co. KGaA.

[17] An, C. M., Sin, W. S., Yoon, J. & Sammes, N. (2010) Fabrication of an Intermediate-Temperature Anode-Supported Planar SOFC Via Tape Casting and Lamination. *Advances in Science and Technology*, volume 72, pp. 237-242.

[18] Winkler, W. & Nehter, P. (2008) Chapter 2, Thermodynamics of Fuel Cells. In *Modeling Solid Oxide Fuel Cells* [Electronic], editors Roberto Bove and Stefano Ubertini, pp. 13-50. Dordrecht: Springer.

[19] Williford, R. E., Chick, L. A., Maupin, G. D. & Simner, S. P. (2003) Diffusion Limitations in the Porous Anode of SOFCs. *Journal of the Electrochemical Society*, volume 150, issue 8, pp.1067-1072.

[20] Larmine, J. & Dicks, A. (2009) *Fuel Cell Systems Explained*. 2nd edition. Chichester: John Wiley & Sons Ltd.

[21] Lee, J.-H., Lee, H.-W., Lee, D.-S., Heo, J.-W., Kim, G.-H., Kim, J., Song, H. S. & Moon, J.-H. (2003) The impact of anode microstructure on the power generating characteristics of SOFC. *Solid State Ionics*, volume 158, issue 3, pp 225-232.

[22] Nordling, C. & Österman, J. (2006) *Physics handbook for science and engineering*. Lund: Studentlitteratur.

[23] Cheng, D. K. (1993) *Fundamentals of Engineering Electromagnetics*. Upper Saddle River, New Jersey: Prentice-Hall.

[24] Zeng, Z & Natesan, K. (2004) Corrosion of metallic interconnects for SOFC in fuel gases. *Solid State Ionics*, volume 167, issues 1-2,pp. 9-16.

[25] Horri, B. A., Selomulya, C. & Wang, H. (2012) Modeling the Influence of Carbon Spheres on the Porosity of SOFC Anode Materials. *Journal of the American Ceramic Society*, volume 95, issue 4, pp 1261-1268.

[26] Albano, M. P., Genova, L. A., Garrido, L. B. & Plucknett, K. (2008) Processing of porous yttria-stabilized circonia by tape-casting. *Ceramics International*, volume 34, issue 8, pp. 1983-1988.

[27] Albano, M. P., Garrido, L. B., Plucknett, K. & Genova, L. A. (2009) Influence of starch content and sintering temperature on the microstructure of porous yttria-stabilized zirconia tapes. *Journal of Materials Science*, volume 44, issue 10, pp. 2581-2589.

[28] Divisek, J., Wilkenhöner, R. & Volfkovich, Y. (1999) Structure of SOFC anode cermets Part 1: Porosity investigations. *Journal of applied electrochemistry*, 29, 153-163.

[29] Archer, W. I. & Armstrong, R. D. (1980) 3. The Application of A.C. Impedance Methods to Solid Electrolytes. In *Electrochemistry*. Editor H. R. Thrisk, pp.157-202. Oxford: Alden Press.

[30] Yuan, X.-Z., Song, C., Wang, H. and Zhang, J. (2010) Electrical Fundamentals. In *Electrochemical Impedance Spectroscopy in PEM Fuel Cells; Fundamentals and Applications*, pp. 39-93, London:Springer.

[31] ETH Zürich (2010) Electrochemical impedance spectroscopy *Nonmetallic inorganic Materials-ETH Zürich*. www.nonmet.mat.ethz.ch/education/courses/ceramic2/EIS.ppt. (2014-06-07)

[32] Muralidharan, V. S. (1997) Warburg impedance – basics revisited. *Anti-Corrosion Methods and Materials*, Volume 44, Issue 1, pp. 26-29.

[33] Yuan, X.-Z., Song, C., Wang, H. and Zhang, J. (2010) Impedance and its Corresponding Electrochemical Processes. In *Electrochemical Impedance Spectroscopy in PEM Fuel Cells; Fundamentals and Applications*, pp. 95-138, London:Springer.

[34] Sanchez-Bautista, C., Dos santos-Garcia, A. J., Pena-Martinez, J. and Canales-Vazquez, J. (2010) The grain boundary effect on dysprosium doped ceria. *Solid State Ionics*, volume 181, issues 37-38, pp. 1665-1673.

[35] Cohen, J. L., Volpe, D. J. & Abruna, H. D. (2007) Electrochemical determination of activation energies for methanol oxidation on polycrystalline platinum in acidic and alkaline electrolytes. *Physical Chemistry Chemical Physics*, volume 9, issue 1, pp. 49-77.